

OPEN ACCESS

EDITED BY Jun Sun, Tianjin University of Science and Technology, China

REVIEWED BY
Peisong Yu,
Ministry of Natural Resources, China
Vincenzo Alessandro Laudicella,
National Institute of Oceanography and
Applied Geophysics, Italy

*CORRESPONDENCE Simón Gutiérrez Duque ☑ gutierrezds@javeriana.edu.co

RECEIVED 23 May 2025 ACCEPTED 25 September 2025 PUBLISHED 30 October 2025

CITATION

Gutiérrez Duque S, Acosta A, Murcia A, Garcia AP, Corredor-Acosta A, Hernandez-Ayon JM, Coronado Álvarez LdLA, Kahl LC and Ruiz-Pino D (2025) Seasonal air-sea CO₂ flux dynamics in Colombia's Gorgona Marine Area during La Niña 2021–2022. *Front. Mar. Sci.* 12:1633653. doi: 10.3389/fmars.2025.1633653

COPYRIGHT

© 2025 Gutiérrez Duque, Acosta, Murcia, Garcia, Corredor-Acosta, Hernandez-Ayon, Coronado Álvarez, Kahl and Ruiz-Pino. This is an open-access article distributed under the terms of the Creative Commons Attribution License (CC BY). The use, distribution or reproduction in other forums is permitted, provided the original author(s) and the copyright owner(s) are credited and that the original publication in this journal is cited, in accordance with accepted academic practice. No use, distribution or reproduction is permitted which does not comply with these terms.

Seasonal air-sea CO₂ flux dynamics in Colombia's Gorgona Marine Area during La Niña 2021–2022

Simón Gutiérrez Duque^{1*}, Alberto Acosta¹, Andrea Murcia¹, Alejandro P. Garcia¹, Andrea Corredor-Acosta^{2,3}, José Martin Hernandez-Ayon⁴, Luz de Lourdes Aurora Coronado Álvarez⁴, Lucía Carolina Kahl⁵ and Diana Ruiz-Pino⁶

¹UNESIS (Unidad de Ecología y Sistemática), Departamento de Biología, Facultad de Ciencias, Pontificia Universidad Javeriana, Bogotá, Colombia, ²División de Investigación en Acuicultura, Instituto de Fomento Pesquero (IFOP), Putemún, Chile, ³Centro FONDAP de Investigación en Dinámica de Ecosistemas Marinos de Altas Latitudos (IDEAL), Instituto de Acuicultura y Ciencias Ambientales, Universidad Austral de Chile, Puerto Montt, Chile, ⁴Instituto de Investigaciones Oceanológicas, Universidad Autónoma de Baja California, Ensenada, Baja California, Mexico, ⁵Departamento Oceanografía, Servicio de Hidrografía Naval, Buenos Aires, Argentina, ⁶Sorbonne Universités (IPSL-CNRS-IRD-MNHN), LOCEAN Laboratory, Paris, France

Air-sea CO₂ fluxes in tropical coastal zones are strongly influenced by ENSO variability, but in situ measurements in the Eastern Tropical Pacific remain scarce. We assessed seasonal CO2 dynamics around Gorgona Island (Panama Bight, Colombian Pacific) under La Niña 2021-2022. From November 2021 to July 2022, we conducted monthly sampling at seven stations spanning the Guapi River plume to the open ocean, measuring physical (SST, SSS, thermocline depth), chemical (TA, DIC, pH, carbonate system parameters), and biological (chlorophyll-a) variables, and estimating net CO₂ fluxes (FCO₂) with the Liss and Merlivat (1986) parameterization and atmospheric CO2 from NOAA. La Niña featured a cool-water anomaly (-0.78 °C), enhanced precipitation (+59%) and river discharge (+44%) relative to multi-year means. The nine-month mean CO₂ flux was near neutral (-0.01049 ± 0.00014 mol C m⁻²) but strongly seasonal: six post-upwelling months showed slightly positive fluxes (0.00929 ± 0.000147 mol C m⁻²) associated with high precipitation (746.4 \pm 214.7 mm), warmer SST (27.5 \pm 0.4 °C), elevated pCO₂w (567 \pm 97.5 μ atm) and lower pH (7.869 \pm 0.040), whereas three upwelling months showed slightly negative fluxes ($-0.00119 \pm$ 0.00010 mol C m⁻²) with reduced precipitation (165.8 \pm 82.4 mm), cooler SST $(26.5 \pm 0.2 \,^{\circ}\text{C})$, lower pCO₂w $(461 \pm 92.8 \,\mu\text{atm})$ and higher pH (7.968 ± 0.048) . La Niña amplified pCO₂w variability (316-839 µatm) via vertical Ekman pumping, horizontal transport (Zonal Ekman Transport, tides), and freshwater inputs, while a persistent thermocline (10-40.1 m) restricted deep CO₂-rich waters from

reaching the surface. Biological uptake further modulated outgassing, as evidenced by chlorophyll-a and ΔDIC dynamics. Overall, CO_2 fluxes were relatively low compared with other tropical estuarine and oceanic sources. These results underscore the need for sustained in situ observations in estuarine–ocean systems to refine predictive models of CO_2 fluxes under ENSO conditions.

KEYWORDS

ENSO, CO₂ Flux, Gorgona, Panama Bight, Eastern Tropical Pacific, estuarine systems, seasonal variability

1 Introduction

Oceanic carbon fluxes have become a central focus in marine biogeochemistry and are increasingly studied for their potential in carbon sequestration (Lal, 2024; Gerrard, 2023; Santos et al., 2022). The oceans absorb around 31% of CO₂ emissions from fossil fuels (Friedlingstein et al., 2023; Parv et al., 2023). However, not all parts of the ocean have the same absorption capacity, with the poles acting as sinks and tropical areas considered sources of CO2 to the atmosphere (Legge et al., 2015; Yilmaz et al., 2022; Swesi et al., 2023). The largest carbon sinks are found in the Arctic and polar waters, with fluxes between -3.8 mol C m⁻² yr⁻¹ and -4.4 mol C m⁻² yr-1-1 (Olafsson et al., 2021), due to carbon "drawdown" from high primary productivity, deep convective mixing, water heat loss and strong seasonal winds (Olafsson et al., 2021). On the other hand, coastal zones, which only contain 7-8% of the ocean's surface area, are nutrient-rich and account for 25% of global primary production (Smith and Hollibaugh, 1993), which allows them to be more effective than the open ocean in retaining the atmospheric CO₂ (Andersson, 2005). However, some coastal tropical areas are sources (Kryzhova and Semkin, 2023) and others are sinks (Roobaert et al., 2021; Watanabe et al., 2024), depending on many factors, which are seldom explored (Chen and Borges, 2009; Borges and Abril, 2011; Cai et al., 2011; Kahl, 2018; Rosentreter et al., 2023; Roobaert et al., 2025). Similarly, in tropical areas, CO2 flux can vary between source or sink depending on atmospheric and oceanographic conditions in space, which also change during different seasons of the year, with the net flux further influenced by complex biogeochemical processes (Monteiro et al., 2022; Swesi et al., 2023).

Among the global drivers of carbon flux, biological processes predominantly influence equatorial and subpolar zones, while sea surface temperature (SST) and salinity (SSS) play a fundamental role in subtropical areas (Roobaert et al., 2021). Additionally, the direction and magnitude of flux in each location depend on atmospheric processes such as wind stress and ENSO events (Ford et al., 2022). La Niña event in particular has a significant effect on the direction and magnitude of CO₂ flux, as it increases coastal upwelling and Ekman pumping (Amos and Castelao, 2022),

enabling outgassing events (facilitating carbon flux to the atmosphere) of around 1 billion tons of carbon (CO₂) per year, where deep waters rich in dissolved inorganic carbon (DIC) rise to the surface. This contrasts with the inherent capacity of coastal upwelling regions to act as significant carbon sinks through the biological pump they promote (Lanson et al., 2009). Moreover, rainfall during La Niña events tends to be more intense (Chung and Power, 2014), shifting coastal systems from upwelling to post-upwelling (river-dominated ocean margin; Dai et al., 2022).

Thus, the ENSO-driven oscillations between cold (La Niña) and warm periods (El Niño) in the Tropical Pacific involve massive redistributions of heat content in the surface ocean (Amos and Castelao, 2022), thereby altering the net carbon flux. Despite this, few studies focus on what happens in the Eastern Tropical Pacific and specifically in the Panama Bight (e.g., Kao and Yu, 2009; Corredor-Acosta et al., 2020; Torres et al., 2023). Recent findings in the Colombian Caribbean indicated that ENSO events are the most important influence over marine biogeochemistry as increased upwelling anomalies bring up water's rich in DIC (Ricaurte-Villota et al., 2025). Therefore, the question arises as to whether the same patterns and drivers apply in the Colombian Pacific as those observed for the Caribbean area.

Latitudinal trends reveal distinct patterns in whether coastal zones act as sources or sink of CO2. In low latitudes, coastal zones are expected to release CO2 due to physical processes such as high sea temperature (average SST above 26 °C) and relatively low salinity (25.7-32 units), which cause higher partial pressures of CO2 in water (pCO2w) compared to the atmosphere (Borges et al., 2005; Cai, 2011). However, whether low latitudes emit CO₂ depends on the drivers in each coastal zone (Dai et al., 2013), and this is why the fine balance between the promoters of pCO_{2w} and those that help to reduce it must be studied locally. For example, in upwelling zones (high DIC and pCO_{2w}), phytoplankton blooms can capture large amounts of CO2, reducing DIC excesses and resulting in exceptionally low pCO_{2w} values, thereby altering the direction of net carbon flux to negative values (Li et al., 2022). According to Strutton et al. (2008), the equatorial Pacific would be a much larger carbon emitter if not for photosynthetic processes, which convert a billion tons of DIC/CO₂ into living organisms.

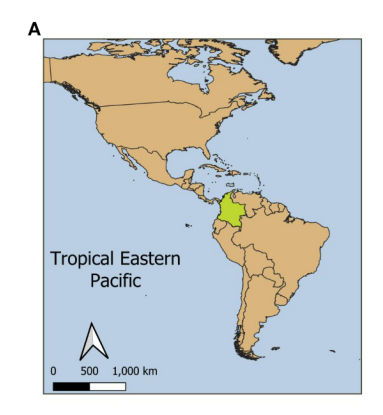
One of the main issues in the Pacific Ocean regarding the net CO₂ flux is the discrepancy between models and *in situ* air-sea CO₂ observations (Polavarapu et al., 2018; Rastogi et al., 2021). This is due to the limited amount of data, particularly in the coastal zones of the Pacific, and specifically in the Panama Bight, which includes the Pacific coast of Colombia and Panama (Herrera Carmona et al., 2022). The uncertainty in predictions stems from the fact that there are many complex atmospheric and oceanographic variables physical (e.g., wind; Takahashi et al., 2002; Kim et al., 2019), chemical (i.e., Total Alkalinity-TA and Dissolved Inorganic Carbon- DIC), and biological (biological uptake, remineralization; Takahashi et al., 1997) that cause significant spatial and temporal variations in pCO_{2w} at different scales (DeGrandpre et al., 1998), and consequently, in the magnitude and direction of the net flux. Moreover, the lack of technical, technological, infrastructural, and financial resources in Latin American countries makes it challenging to quantify pCO_{2w} values and the magnitude of the flux, particularly in the coastal zone, where multiple drivers converge in time and space (Roobaert et al., 2024).

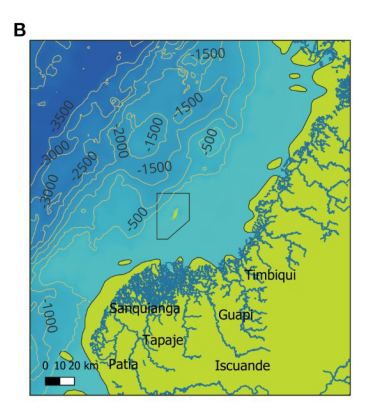
According to Dai et al. (2022), calculating pCO_{2w} and CO₂ flux in tropical coastal margins dominated by rivers and deltas is particularly complex. The dissolved inorganic carbon (DIC), dissolved organic carbon (DOC; 49.5% of DOC export is by rivers concentrated in the tropics, 23.5°S to 23.5°N; Fabre et al., 2020), particulate organic matter (POM), dissolve organic matter (DOM), and nutrients (NO₃ and PO₄; Li et al., 2020) are mainly contributed by rivers. These contributions promote phytoplankton growth (a CO₂ sink) and the consequent remineralization of dead particulate organic matter (a CO₂ source), where the resultant flux is the product of all these interactions. In a system with predominant river inputs, the fresher waters of the river plume gradually mix with oceanic waters both horizontally and vertically (Gan et al., 2009), creating an estuarine ecosystem, like the one found in the Colombian Pacific around Gorgona Island. In consequence, Dai et al. (2022)

suggest that the air-sea CO2 flux is determined by the sum of DIC inputs and outputs at the coast-ocean boundary over time, net ecological productivity (gross primary production - ecosystem respiration), and net ecological calcification (Andersson and Gledhill, 2013; Courtney and Andersson, 2019). However, systems dominated by river inputs can transition to predominantly oceanic inputs depending on the water volume it receives from the open sea, for example, during coastal upwelling events (Ekman Pumping -WEK) and horizontal transport (Zonal Ekman Transport - ZET) when cold, CO₂- and DIC-rich subsurface ocean water emerges (Hu et al., 2015; Weber et al., 2021), or through surface water movement by ocean currents toward the coast and tides. Changes from a river to oceanic coastal regimes and vice versa alter the direction and intensity of the CO2 flux and should be explored further according to Dai et al. (2022). This is the reason why this study focuses on the Gorgona's continental island, located 55 km from the continent but strongly influenced by many rivers, upwelling events and sustained primary productivity (Corredor-Acosta et al., 2020).

The Gorgona Island (2° 55' 45" – 3° 00' 55" N; 78° 09' – 78° 14' 30" W; Figure 1) is located on the continental margin of the Colombian Pacific Basin (CPB) in the Panama Bight region, and is part of the largest Marine Natural National Park in the Colombian Pacific (Guzmán et al., 2023; UAESPNN, 2005). The island is characterized by a wide and shallow continental shelf to the east (less than 100 m deep; Figure 1) and a deep slope a few kilometers to the west, with canyons and submarine mountains according to Murcia and Giraldo (2007; Figure 1B).

Precipitation on Gorgona Island follows a bi-seasonal pattern (periods of less and more rain), with an annual total rainfall up to ~6000 mm (Blanco, 2012). At seasonal scale, we performed a multi-year analysis of precipitation on the Gorgona Island (2006-2021, data source IDEAM) which indicated low relative rainfall from January to April (Figure 2), when the northern trade winds dominate and the wind field of the Chocó Jet is weak. In contrast,





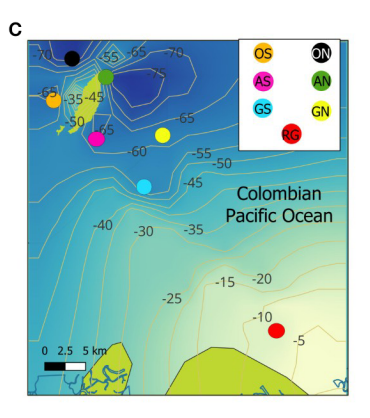
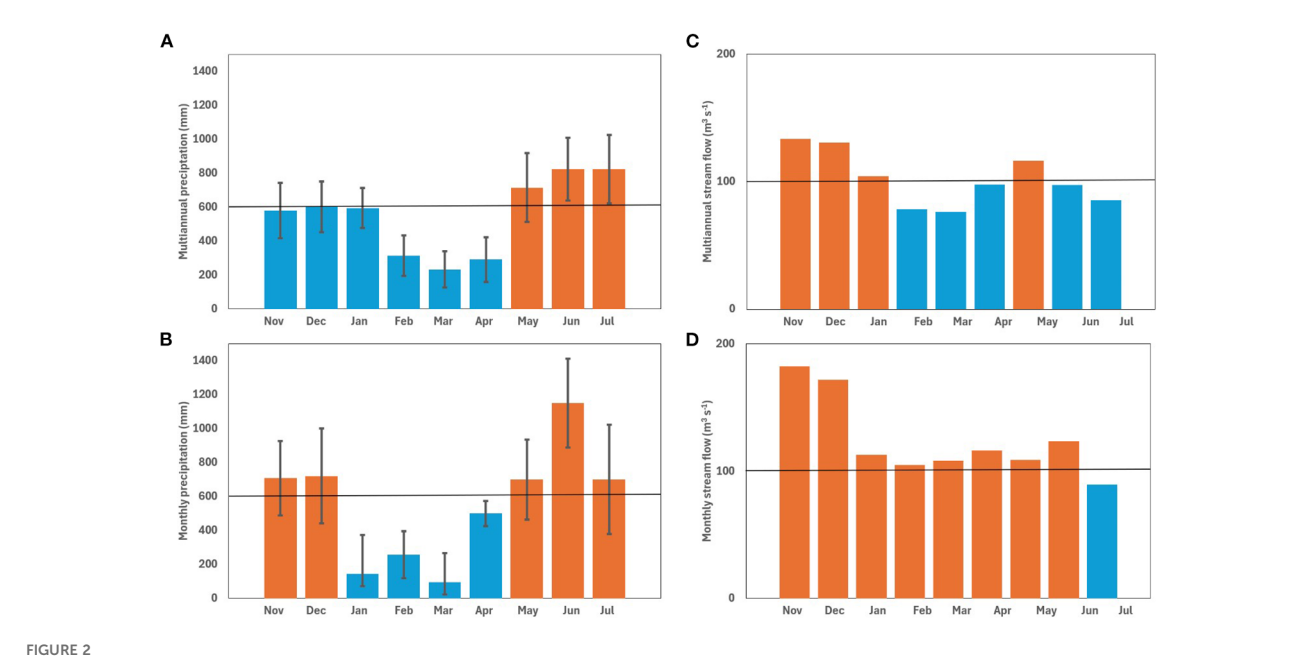


FIGURE 1

The study area is the Colombian Pacific Ocean (Tropical Eastern Pacific). (A) Location of the Colombian Pacific, as part of the Panama Bight. (B) The polygon representing the protected area of the Gorgona National Natural Park is shown, along with its proximity to the coastline and the main continental watersheds that discharge their waters into the area (marked in blue): Patía River, Sanquianga River, Tapaje River, Iscuandé River, Guapi River, and Timbiquí River. (C) The colored points show the seven stations where discrete water samples were collected from November 2021 to July 2022 along the coast-ocean gradient; Guapi River in red (RG), South Guapi in blue (GS), North Guapi in yellow (GN), South Reef in pink (AS), North Reef in green (AN), South Ocean in orange (OS), and North Ocean in black (ON). The underwater topography lines are represented in meters.



Time scale comparison of precipitation and streamflow (Río Guapi) in the study area. (A) Multiannual total precipitation as monthly averages (2006-2021). The black horizontal line marks the historic (2006-2021) annual mean total precipitation (605 mm) for the "Isla Gorgona station". Standard deviation is illustrated on each month's data. (B) Average monthly total precipitation for the sampled year (November 2021 to July 2022). Black horizontal line marks the historic annual mean (2006-2021). Standard deviation is illustrated on each month's data. (C) Multiannual total streamflow as monthly averages (2006-2021) from the "57025020 Isla Gorgona" IDEAM station. Black horizontal line marks the historic (2006-2021) annual mean discharge (103 m $^{-3}$ s $^{-1}$). (D) Average total monthly streamflow for the sampling year (November 2021 to July 2022) at the "53047010 Río Guapi" station of IDEAM. Black horizontal line marks the historic (2006-2021) annual mean discharge (103 m $^{-3}$ s $^{-1}$). Months below the multiannual records are shown in blue, and above in orange.

the period with higher precipitation conditions were found from May to December (not shown), when the southern trade winds dominate and the Chocó Jet winds are stronger (September to October). Figure 2 shows extreme precipitation during the 2021-2022 sampling year, with monthly rainfall exceeding 700 mm for several months. Only four months recorded precipitation below the multiannual average (Figure 2B). The precipitation regime on Gorgona Island is primarily governed by the latitudinal migration of the Intertropical Convergence Zone (ITCZ), which provides the context for understanding the atypical precipitation observed. According to Schneider et al. (2014), this pattern dictates that the relative driest period occurs in January and February, when the ITCZ is at its southernmost position (2°N) near the study area (2° 55' - 3° 00'). Then, from March to May, it moves to the north, occupying a latitudinal range between 2 and 7°N. Conversely, the wettest period is expected between June and July as the ITCZ moves north (reaching 8 to 10°N). Finally, between September and December, the ITCZ returns to its southernmost position.

In the study area, the northeastern trade winds dominate between December and March, generating the Panama Jet, which causes a strong upwelling extending from north to south in the Panama Bight (Rodríguez-Rubio et al., 2003; Corredor-Acosta et al., 2020; Crawford et al., 2023). Similarly, in the second half of the year, the Chocó Jet occurs (Rodríguez-Rubio et al., 2003; Crawford et al., 2023), which travels from west to east until it collides with the continent. The Chocó Jet is strongest in November and weakest between February and March, so the heavy rainfall from November

to December on Gorgona Island is attributed to this climatic phenomenon (Crawford et al., 2023). The intense rain creates a layer of brackish water on the surface, up to 2 meters thick (Gassen et al., 2024), which reduces salinity on the Colombian Pacific coast, and river runoff from the Guapi river and deltaic complex into the sea increases. The Guapi River characterized by a sea water temperature of 26.34 °C at 10 meters (Palacios Moreno and Pinto Tovar, 1992), had an average NBS pH of 7.3 between 2018 and 2021, and salinity (PSU) between 0 and 0.25 at 1-meter depth (INVEMAR, 2019, 2020, 2022).

The island is influenced to the east by several rivers and deltas from the mainland, and on the oceanic side (west) by oceanic currents from the Northern Hemisphere, such as the California and Northern Equatorial currents, and from the Southern Hemisphere, by the Peru and Humboldt currents (Diaz, 2001; Willett et al., 2006; Fiedler and Lavin, 2017). The hydrodynamic pattern around the island is dominated by ocean currents and numerous mesoscale eddies, both cyclonic and anticyclonic occurring throughout the year. The direction and intensity of those geostrophic field and mesoscale eddies around Gorgona are determined by wind stress, the Panama Jet, the Chocó Jet, and the position of the Intertropical Convergence Zone (Rodríguez-Rubio et al., 2003; Díaz Guevara et al., 2008; Corredor-Acosta et al., 2011; Lorenzoni et al., 2011). Specifically, the Panama cyclonic current (Amaya, 2024) is fed from the south by a branch of the Peru current, forming the so-called Colombia current (Stevenson, 1970; Corredor-Acosta et al., 2011), which flows from south to north along the Colombian coast. The

surface water masses flows through the area of Gorgona National Natural Park in a northeastward direction, with a velocity ranging between 0.2 and 0.9 m s⁻¹ (Diaz, 2001). During La Niña, the North Equatorial Countercurrent (warm water with high salinity) flowing from west to east (Torres et al., 2023) loses it prevalence around 3° N, while the Peru Current, flowing in a northeastward direction, brings cold water from the South Pacific to the Colombian coast. Therefore, the sampling carried out in this present study (2021-2022) corresponds to a period of relatively cold water (La Niña; ONI -1.0; McLean et al., 2024) contrasting with what happens during El Niño events. Also, at more local scale, the oceanographic circulation is affected by semidiurnal tides (two highs and two lows) oscillating between -40 cm and 5 m per day (Tide-Forecast.com, map of tide stations in Colombia 2021-2022).

According to Restrepo and Kjerfve (2004) and Blanco (2012), La Niña events significantly influences river discharge in the Colombian Pacific due to increased precipitation and, consequently, water flow especially during the sampled year (Figure 2). The Colombian Pacific watershed covers an area of 76,852 km² and consists of more than 200 rivers, which a total discharge of ~9,000 m³ s⁻¹ and 96 million tons of sediment per year (Díaz, 2008). The Gorgona National Natural Park is in front of the Patía-Sanquianga delta complex, the largest in the country, which contributes approximately 23% of the total freshwater discharged into the Colombian Pacific (2,045 m3 s-1; Díaz, 2008). The delta complex is made up of the Patía-Sanquianga rivers, which discharge 1,300 m³ s⁻¹, the Guapi River at 357 m³ s⁻¹, the Iscuandé River at 213 m³ s⁻¹, and the Tapaje River at 175 m³ s⁻¹ (Restrepo and Kjerfyel, 2004; Díaz, 2008; Figure 1). The Patía-Sanquianga delta, covering an area of 23,000 km², contributes freshwater, nutrients, and organic and inorganic material (both particulate and dissolved) from the western Andes mountains to the Pacific Ocean (Restrepo and Kjerfve, 2004; Giraldo et al., 2011). The Guapi River multi-year average monthly flow (station "53047010 IDEAM") was 103 m³ s⁻¹ from 2000 to 2021. However, during La Niña event (2021-2022), the stream flow exceeded the multi-year monthly average, with a maximum value in November 2021, exceeding the average by over 77% (182 m³ s⁻¹), with a minimum in February 2022 being also 2% above the multi-year monthly mean (105 m³ s⁻¹; Figure 2). On average, the flow exceeded expectations, except for July 2022 when it was 14% below the multi-year average (89 m³ s⁻¹).

In this context, this study aims to: (1) evaluate the net CO_2 flux in the Panama Bight to address a gap in the current knowledge of the region, as no similar studies have been addressed it in the coastal zone of the Colombian Pacific; and (2) review the predictions made by the models proposed by Wong et al. (2022) and Dai et al. (2022), assessing their accuracy and applicability in the context of this study. To do so, we estimate the seasonal direction and intensity of the CO_2 flux under the effects of La Niña conditions (2021-2022), characterized by intense precipitation and river discharge promoting an estuarine system. Lastly, we discuss the potential drivers explaining the dynamics of the pCO_{2w} and CO_2 flux variability.

2 Methods

2.1 Sampling design

Seven stations were sampled and used to estimate CO₂ fluxes and carbonate system chemistry in Gorgona National Natural Park from the coast to the open ocean. The closest station to the coast was "Río Guapi - RG", located approximately 25 km from Guapi-Nariño, Colombia, and the furthest was "North Ocean - ON", approximately 60 km from the coastline. The stations were distributed along two parallel transects separated by five kilometers, with GPS-WGS84 coordinates. The southern transect was formed by "South Guapi - GS", "South Reef - AS", and "South Ocean - OS", while the northern transect was formed by "North Guapi - GN", "North Reef - AN", and "North Ocean - ON" (Figure 1). Monitoring began in November 2021 and extended until July 2022 (nine months), with monthly sampling during the first week of each month. In addition, the "Río Guapi" station was added in January 2022 to characterize its influence.

2.2 Measurements

On site, salinity, temperature, pH millivolts (total protons), percent oxygen, and depth were measured using a Hanna multiparameter sounder (previously calibrated), a CTD-Castaway, and a YSI equipment (accurate to $\pm 2\%$ of reading or ± 0.01 PSU, whichever is greater; ± 0.15 °C; ± 0.02 pH/ ± 0.5 mV; and ranging from 0.00 to 30.00 ppm (mg/L) with an accuracy of $\pm 0.25\%$ of full range.

Discrete water samples were collected at seven stations (GS, GN, AS, AN, OS, ON, and RG; Figure 1) using a 5 L Niskin bottle at depths between 1.8 and 3 meters. The water collected on site was not murky, sampling sites were right after the river plume limit (35 km away from the continent). Seawater samples were stored in 250 mL borosilicate bottles and preserved with 50 μL of a saturated mercuric chloride (HgCl2) solution for later TA analysis in the laboratory, following recommended best practices (Best Practice Guide for Ocean CO2 Measurements, SOP 2, SOP-specified concentration range of 0.02-0.05%). Additionally, DIC samples were taken in 50 mL dark bottles (silicone seal), leaving no headspace; and wrapping the cap in parafilm paper. All samples were packed in a Styrofoam refrigerator and sent by plane to our new lab in Bogotá (Javeriana University) in less than four hours from the Pacific region. Then, the samples were kept without exposing them to light and maintaining temperature conditions below 15 °C in the laboratory. TA was measured within two weeks, as well as other parameters such as pH. Regarding DIC samples, those were kept in our lab for two months after the sampling was finished and then sent to the Autonomous University of Baja California in Mexico. They were processed in a maximum of one week after arrival in the UABC.

In the laboratory, total alkalinity (TA) measurements were performed on seawater samples following a standardized protocol (SOP 3b of the open-cell titration method; Dickson et al., 2007) using the GOA-ON titration kit. For titrant, Dickson Lab reference HCl solutions were used (Batch A17: $0.100362 \pm 0.000009 \text{ mol kg}^{-1}$; Batch A24: 0.099922 ± 0.000005 mol kg⁻¹), buffered with 0.6 M NaCl to match seawater ionic strength. A 50 g sample (~50 g or mL, ± 0.0001 mL) was weighed into a jacketed titration cell (maintained at ~25 °C via a circulating water bath) and titrated. The analytical balance used (Ohaus Pioneer AX225D, ± 0.0001 g) yielded a reproducibility of ±0.001 g for 50 g samples, corresponding to a coefficient of variation<0.003%, well within the precision requirements for TA analysis (0.01 g). The titration involved two stages: first, the addition of a small amount of acid (0.2 mL) with a HandyStep® Touch S, first by adding to drop the pH to ~3.5 (~0.2100 mV) and waiting 5 minutes to allow for degassing, and second, titration resumed in 0.05 mL steps until a pH close to 3.0 was reached (~0.2300 mV), with pH and temperature measurements taken at each step. Data, including sample volume, titrant volumes (to pH 3.5 and 3.0), salinity, final temperature, and voltage per addition was compiled in an Excel spreadsheet program, which employed a non-linear least squares regression to calculate total alkalinity (Dickson et al., 2007). Approximately 50% of surface samples (n = 31) were analyzed in triplicate. Only triplicate sets with a maximal variation of ±5 μmol kg⁻¹ TA were retained (± 9 μmol kg⁻¹ 1 , Batch #182: 2230.91 \pm 0.71 μ mol kg $^{-1}$; Batch # 202: 2215.13 \pm 0.57 μmol kg⁻¹; all data set available at NOAA; https://doi.org/10.25921/ gfan-3e30).

Dissolved Inorganic Carbon (DIC) was measured at UABC (Mexico) using the UIC C-CM5014 instrument, following the coulometric methodology described by Johnson et al. (1987) and Dickson et al. (2007). Measurements were performed with high precision and accuracy, ensuring that the difference in DIC from the reference values of the standards did not exceed 3 µmol kg⁻¹ (error of 0.1%). The Dickson Certified Reference Material (CRM) was prepared at the Institute of Oceanography, University of California, San Diego (USA). The substandards and analyzed samples were carried out in parallel at the Oceanographic Research Institute of the Autonomous University of Baja California (Mexico). For a more comprehensive DIC measurement methodology, see Supplementary Table 1.

Similarly, quality "flags" (scale 1 to 5) were reviewed and assigned to the TA and DIC data (equipment accuracy and potential errors in the field or laboratory). Outliers (n=6) were removed from the matrix; this was done by reviewing multiple graphical relationships between temperature, salinity, TA, and DIC.

The Liss and Merlivat (1986) equation allowed for the calculation of the flux magnitude for each of the nine months and seasons in Gorgona. The estimated CO₂ flux in Gorgona was compared with the IPACOA, OOI, NOAA, and SOCAT databases.

The CO₂ fluxes (FCO₂ direction, magnitude, and variability) were calculated following the equation proposed by Liss and Merlivat (1986):

$$FCO_2 = k \times K' \times (\Delta pCO_2)(mmol \cdot m^2 \cdot year^{-1})$$

Where, the constant k is the gas transfer coefficient of CO₂ as a function of wind (U₁₀) at 10 meters above sea level (Wanninkhof, 2014), expressed as:

$$k = 0.251 \left(\frac{Sc}{660}\right) 0.5 (U_{10})^2$$

K' is the solubility of CO_2 and is a function of temperature and salinity (Weiss, 1974); Sc is the Schmidt number and depends on temperature; ΔpCO_2 is the difference between the partial pressure of carbon dioxide (pCO₂) in the surface seawater (pCO_{2w}) and the pCO₂ of the atmosphere (pCO_{2A}). ΔpCO_2 determines the direction of the flux, with positive FCO₂ indicating CO₂ moving from the sea to the atmosphere, and negative indicating movement from the atmosphere to the sea. The magnitude of the gas exchange is controlled not only by ΔpCO_2 but also by the gas transfer rate between the two media, which in turn varies with wind speed.

The hourly wind speed from the seven sampling sites - U_{10} (m s⁻¹) was extracted from: https://earth.nullschool.net/, taking the 24-hour wind average of the sampling day. For months with sampling of all stations on two consecutive days (adverse weather conditions in two months), 48-hour wind values were averaged. The wind average was also calculated and compared using only the exact sampling hours at each station and by averaging the wind over a month, finding no significant changes in the flow results compared to the daily/monthly wind average (which was finally used).

Since the atmosphere is a well-mixed fluid, the pCO $_{2A}$ values for the flow calculation were extracted from NOAA/GML https://gml.noaa.gov/ccgg/trends/data.html (NOAA 2021, 2022), which come from the Mauna Loa climate station, Hawaii, file "Mauna Loa CO $_{2}$ monthly mean data." The pCO $_{2A}$ data for the sampling months (Nov 2021 to Jul 2022) were extracted.

The pCO_{2w} was calculated from TA, DIC, salinity, and temperature data resolving the carbonate system equation in seawater using the CO2SYS v3.0 software (Pierrot et al., 2021). In the carbonate system equation solution, the following constants were used: (i) Dissociation constants for K1 and K2 from Millero (2010) for waters ranging from 0 to 40, given that the study area the salinities variation are between 27.03 to 31.29, (ii) KHSO4 dissociation constant from Dickson (1990), (iii) KHF from Perez and Fraga (2003), (iv) Total pH scale (mol-kg SW), (v) [B]T value from Lee et al. (2010), and (vi) EOS-80 standard. The pCO_{2w} was estimated with an error of ±1.79 concerning the determined fluxes (mmol C m² day⁻¹). Out of 66 flux data points, six were flagged as possible outliers (flags three onward). The CO2SYS was also used with DIC and TA pairs to estimate the Revelle factor, omega aragonite (Ω_{AR}), HCO₃, and CO₃. Lastly, the pH in total scale was derived through the CO2SYS using the same specific settings and found to be less variable than in situ measurements, displaying a smaller error. We performed a full uncertainty propagation analysis, which yielded the following average errors: pH_T (± 0.022), pCO_{2W} (\pm 30.17 μ atm), total alkalinity (TA: \pm 9 μ mol kg ¹), dissolved inorganic carbon (DIC: ± 3 μmol kg⁻¹), salinity (± 0.20 PSU), and temperature (± 0.08 °C). These values fall within acceptable ranges for carbonate system studies and support the reliability of our calculated FCO2 values at Gorgona.

Daily images of Chl-a were downloaded from the Ocean Colour Climate Change Initiative (OC-CCI; version 3.1) for the studied period. The OC-CCI is a merged Level 3 product with a spatial resolution of 4 km, available at http://www.oceancolour.org/. The OC-CCI Chl-a dataset is retrieved by combining the observational data from the MERIS (MEdium spectral Resolution Imaging Spectrometer) sensor of the European Space Agency, the SeaWiFS (Sea-viewing Wide-Field-of-view Sensor) and MODIS-Aqua (Moderate-resolution Imaging Spectroradiometer-Aqua) sensors from the National Aeronautics and Space Administration (NASA-USA), and the VIIRS (Visible and Infrared Imaging Radiometer Suite) from the National Oceanic and Atmospheric Administration (NOAA-USA). The remote sensing reflectance data derived from the sensors were merged by band-shifting and biascorrecting the MERIS, MODIS, and VIIRS data to match the SeaWiFS data. Due to the complexity of the study region, version 3.1 of the OC-CCI product was selected as it improves the performance of the ocean color data in coastal Case-2 waters compared to earlier versions that primarily focus on open ocean waters. Finally, total monthly Chl-a values were obtaining by averaging the Chl-a of the seven sampling stations, resulting in a relative total Chl-a concentration for the entire sampling region.

2.3 Statistical analyses

The analysis began with a Shapiro-Wilk test, which indicated that the flux magnitude data does not follow a normal distribution (S-W, P = 0.01877, W = 0.95, n = 60), repeating this for pCO_{2w} and ΔpCO_2 components, respectively (S-W, p = 0.147 and 0.134, W = 0.97 and 0.96, n = 60 and 60), indicating that the variables associated with flux do not follow a normal distribution either. Hence, the Box-Cox methodology was applied to transform FCO₂ data into a normal distribution. Furthermore, a Welch F test in the case of unequal variances was applied to all the variables of interest (FCO₂, pCO_{2w}, ΔpCO₂, SST, SSS, TA, DIC, and Chl-a) which showed that these different data groups have equal variance (W-F, F = $2.512E^{-4}$, df = 200.3, p = $1.855E^{-304}$). Moreover, a t-test (parametric) was used to analyze differences between the two flux periods: Upwelling (January to March of 2022) and Post-upwelling (November to December of 2021 and April to July of 2022). We used a One-way ANOVA to compare different flux magnitudes across the nine months, and then an a posteriori t-test. Additionally, a Spearman linear correlation was run to explore relationships between pCO_{2w} and SST, SSS, TA, DIC, and Chl-a.

Normalizations to observe the pCO $_{2w}$ sensitivity were conducted as follows: we used the maximum values for salinity and temperature (32.06 units and 28.1 °C, respectively) setting the maximum value for salinity first, as a constant, while leaving the TA, DIC, and temperature values corresponding to each data point to evaluate the effect of salinity over the pCO $_{2w}$, repeating the same process but substituting the temperature for the recorded maximum, and leaving salinity as measured (CO2SYS). Then, we recalculated the pCO $_{2w}$ and plot the difference between the pCO $_{2w}$

with *in situ* salinity against the recalculated pCO $_{2w}$ that uses the maximum recorded salinity. 49 μ atm higher, in average, was the pCO $_{2w}$ difference by using max salinity effect. Regarding a normalization with maximum temperature, the same procedure was followed where the maximum recorded temperature was constant, and the remaining variables used the corresponding values, revealing an average pCO $_{2w}$ difference of 31 μ atm higher than with the observed temperatures (Supplementary Figure 1) in the CO2SYS (Lewis and Wallace, 1998). Thus, it is clear that salinity has a larger influence (relative percentage) than temperature regarding the pCO $_{2w}$ variability observed throughout the year. To complement these normalizations, we assessed the uncertainty associated with pCO $_{2w}$ by incorporating the potential error of ± 30.17 μ atm into our flux calculations, recalculating them and comparing them to the original estimates.

In addition, to define climatic-oceanographic periods, a Principal Component Analysis (PCA) was performed using the latest version of R Studio software. The PCA used the following variables: month, season, SST, SSS, pCO₂w, pH_T, DIC, Chl-a, to review if there are spatio-temporal FCO₂ groups. Furthermore, to clearly separate both seasons we used several atmospheric/climatic variables, such as total monthly precipitation (mm), average sea surface temperature (SST), average pH (total), average surface water partial CO₂ pressure (pCO_{2w}), and average CO₂ fluxes (mmol m⁻² d⁻¹).

2.4 Zonal Ekman Transport and Ekman pumping

The Zonal Ekman Transport (ZET) was obtained following the methodology of Bakun and Nelson (1991) by using weekly wind data obtained from the CCMP product (https://www.remss.com/measurements/ccmp/). For the calculation, we follow the equation:

$$ZET = \frac{1}{\rho_w f} \tau$$

where ρ_{ω} is the density of seawater, which is assumed constant at 1025 kg m⁻³; f is the Coriolis parameter and τ is the wind stress for the studied area.

The wind stress (τ) was computed from the weekly wind fields as follows:

$$\tau = \rho_a C_d |V_{10}| V_{10}$$

where $C_d = 0.0015$ is the drag coefficient, $\rho_a = 1.2$ kg m⁻³ is the mean air density, and V₁₀ is the wind speed at 10 m above the sea surface. The wind stress curl was estimated using the zonal and meridional components of the weekly wind stress:

$$(\nabla \times \tau)_z = \frac{\partial \tau_y}{\partial x} - \frac{\partial \tau_x}{\partial y}$$

This procedure was performed for each grid point of the wind field by applying the centered finite difference algorithm, and the Ekman pumping velocity was estimated as follows:

$$WEK = \frac{(\nabla \times \tau)_z}{f\rho_w} + \frac{\beta \tau_x}{f^2 \rho_w}$$

where τ_x is the zonal wind stress component, $\beta = (2\Omega\cos\varphi/R)$ is the latitudinal variability of the Coriolis parameter ($f = 2\Omega \sin\varphi$), R = 6,371,000 m is the radius of the earth and $\rho_w = 1025$ kg m⁻³ is the mean water density. This methodology has been previously used on the Northeast Tropical Pacific (Kessler, 2006) and Panama Bight region (Devis-Morales et al., 2008; Corredor-Acosta et al., 2020).

Previous studies have indicated an interplay between the Ekman transport due to alongshore winds and Ekman pumping due to offshore wind stress curl playing an important role due to their relative contributions for upwelling/downwelling dynamics. For instance, in the northern Chilean upwelling system, the vertical transport induced by coastal divergence (ZET) represented the 60% of the annual total upwelling, however, the Ekman pumping also displayed an important contribution of 40%, indicating that the largest differences between these mechanisms occur at spatial scale. That is, coastal ZET predominated in areas with low orography and headlands, whereas WEK was higher in regions with high orography and the presence of embayments (Bravo et al., 2016). Similar findings were observed in three typical upwelling systems of the South China Sea, showing temporal and spatial differences, highlighting regions where WEK had the same intensity as ZET, even doubling the amount of upwelling predicted solely considering the coastal divergence (Wang et al., 2013). Those physical mechanisms and their coupling are important to be explored because the physical transfer of water properties and nutrients from the deep to the surface ocean is strongly related to the vertical supply, which also involves important effects on primary productivity, changes in the water column mixing/stratification and associated water masses, as well as, in the local chemical processes (e.g., Williams and Follows, 2003; Pasquero et al., 2005). According to this, we assess both mechanisms (ZET and WEK) in this study, in order to relate its contributions to the maintenance of biological production (in terms of Chl-a) and key changes of the carbonate system.

2.5 Mix model

To identify potential processes (physical mixing and biological) and explain the variability observed in carbonate system parameters (e.g., pCO_{2w}, DIC, TA, and O₂), we employed a three-endmember mixing model following established methodologies in oceanographic studies that developed the analysis of sea water from mixing triangles without assumption of isopycnic mixing (Tomczak, 1981; Paulmier et al., 2011; Kahl et al., 2018). This approach identifies water endmembers, in order to describe the thermohaline variability due to mixing, using conservative tracers (salinity and potential temperature) to construct a mixing triangle. The contribution of the water masses considered ($M_{k,i}$) to a given sample 'i' can be calculated by solving the followings determined system of three linear equations:

$$1 = \sum_{i} M_{K,i}$$

$$S_i = \Sigma \ M_{K,i} \cdot \ S_k$$

$$\theta_i = \sum M_{K,i} \cdot \theta_k$$

Where k is the water mass endmembers (1,2 and 3) and 'i' is the sample number (from 1 to 60). S_k and θ_k are the thermohaline characteristics of the k-water mass endmember (Tomczak, 1981). Finally, it computes expected conservative values due to physical mixing processes (DIC_{mix}, TA_{mix}, and O_{2mix}) for the nonconservative variables measured in situ (DIC, TA, and O2). DICmix is defined as the fraction of dissolved inorganic carbon whose variability (R2 from the regression DICmix vs. DIC) can predominantly be attributed to physical mixing. The complementary variability (1 -R2) is then attributed to biogeochemical processes, isolated through residual analysis (e.g., ΔDIC = observed DIC - DIC by mixing) and quadrant plots of ΔDIC vs. ΔO_2 , where quadrants indicate net production (positive ΔDIC , positive ΔO_2), photosynthesis (negative Δ DIC, positive Δ O₂) ammonification (negative Δ DIC, negative Δ O₂) or respiration/remineralization (positive Δ DIC, negative Δ O₂) (Paulmier et al., 2011; Kahl et al., 2018).

Initially, we constructed T-S diagrams from the full spatiotemporal dataset (13 months, 7 stations, 0-80 m depth) to define three endmembers representing distinct sources of variability and mixing in the area. The river endmember (1; river-influenced) exhibited low salinity (26.81), TA (1750 µmol kg⁻¹), and DIC (1763 μmol kg⁻¹), with high temperature (27.94 °C) and O₂ (174 μmol kg⁻¹) 1). The transitional endmember (2) showed intermediate values: salinity (33.06), TA (2138 μmol kg⁻¹), DIC (1867 μmol kg⁻¹), temperature (27.28 °C), and O2 (123 µmol kg⁻¹). Finally, the oceanic endmember (3; oceanic influenced) featured high salinity (35.38), TA (1999 μmol kg⁻¹), and DIC (1989 μmol kg⁻¹), with low temperature (14.26 °C) and O2 (40 µmol kg-1; Preciado et al., in Progress). All three water endmembers incorporate signals from multiple upstream sources, reflecting the complex dynamics of this estuarine system. For instance, the oceanic (3) endmember exhibited influence from at least four diverse origins, including Antarctic Intermediate Water signals (Kawabe and Fujio, 2010); the intermediate endmember (2) blends subsurface and riverine inputs; and the river endmember (1) primarily mixes freshwater with marine waters, potentially including remote eddy-transported surface waters and local coastal currents. We could not directly measure riverine carbonate parameters due to differences in instrumentation and chemistry, river itself even showed tidal intrusion of seawater from below during high tides, further complicating pure freshwater end-member isolation. Instead, riverine influence is inferred through its dilution effects on salinity and biogeochemistry, following a similar approach to Huang et al. (2022) and Sun et al. (2023).

Once the mixing fractions are applied to compute expected $\mathrm{DIC}_{\mathrm{mix}}$ values under conservative mixing assumptions. Deviations from these expected values then highlighted non-conservative processes affecting DIC, which is a key objective of our biogeochemical analysis. DIC, TA, and O_2 are used as complementary information for the characterization of the

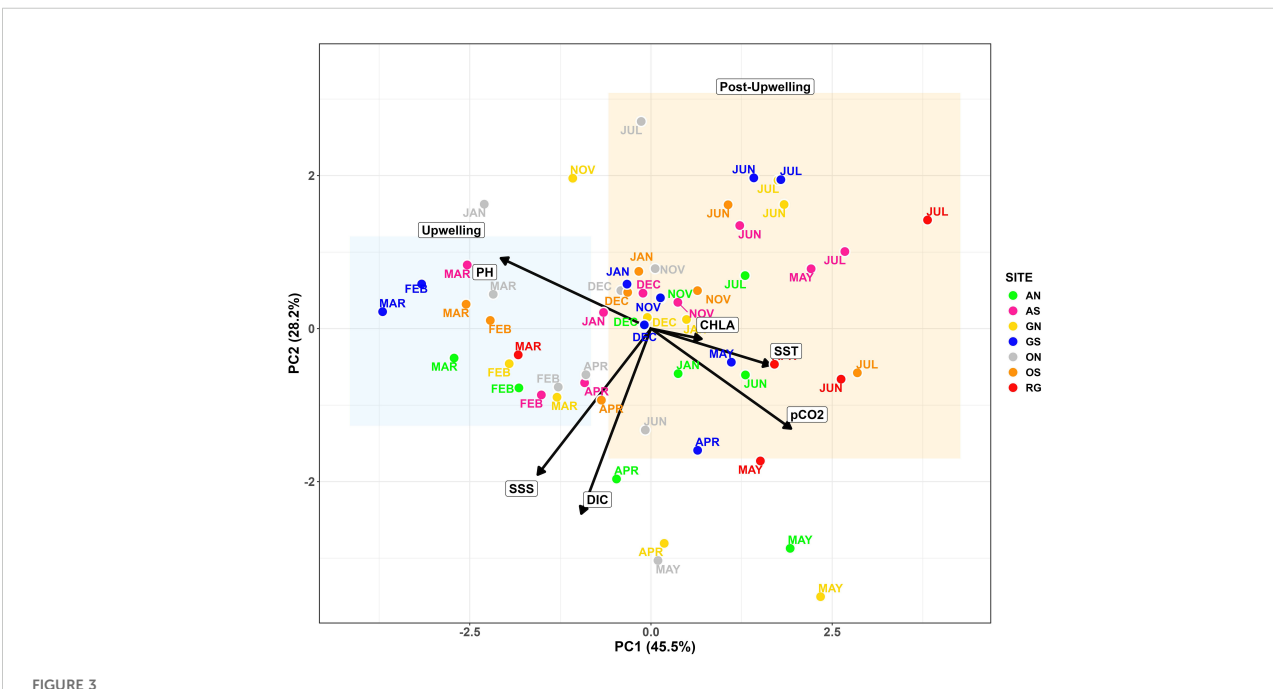
endmembers, enabling us to perform the mixing model analysis and determine the sources of variability (physical-mixing or biogeochemical processes) for the non-conservative variables DIC, TA, and O2. This approach aligns with standard practices in estuarine and oceanic studies, where salinity and TA are often normalized or used to account for dilution and mixing effects before assessing non-conservative variables like DIC (Cai & Wang, 1998; Oliveira et al., 2017; Courtney et al., 2021). For instance, while TA behaves conservatively in many open-ocean settings and correlates linearly with salinity (Millero et al., 1998; Jiang et al., 2014), the T-S framework was chosen due to its effectiveness in capturing thermohaline distinctions in Pacific Colombian dynamic estuarine system, influenced by high rainfall and runoff. In addition, to validate the implication of the biological removal in pCO_w concentration, we used a complementary approach, such as ΔDIC together with cumulative monthly in situ Chl-a data to explain CO2 consumption. These results (biological/temperature implications) were also validated by an analysis to calculate if physical or biological factors are implicated in the pCO_{2w} concentrations found around Gorgona island, following the methodology described by Takahashi et al. (2002), for more detail on the equations used see Supplementary Table 2.

3 Results

The PCA (Figure 3) revealed two distinct seasonal clusters: an upwelling period (January–March) and a post-upwelling period (May–July, November–December) distributed across the space.

Together, PC1 (45.5%) and PC2 (28.2%) explained 73.7% of the total variability. The biplane shows that post-upwelling months were characterized by warmer, CO_2 -enriched surface waters, whereas upwelling months reflected cooler, saltier, DIC-rich conditions and elevated pH_T. Chlorophyll-a displayed an intermediate position, reflecting its role across both seasons. No spatial separation among sampling sites was detected, implying that despite local variability, temporal changes through upwelling and post-upwelling dynamics (e.g. rainfall and stratification) were the main driver of environmental variability around Gorgona Island.

The two seasonal periods were verified through the atmospheric/climatic variables showing significant differences between upwelling and post-upwelling. That is, total monthly precipitation (M-W, Z = 2.203, p = 0.027, n Post-upwelling = 6 months, n Upwelling = 3), average sea surface temperature (SST; M-W, Z = 2.2132, p = 0.0268, n Post-upwelling = 6, n Upwelling = 3),average pH (total; M-W, Z = 2.2039, p = 0.027532, n Post-upwelling = 6, n Upwelling = 3), average surface water partial CO₂ pressure $(pCO_{2w}; M-W, Z = 2.1947, p = 0.028186, n Post-upwelling = 6, n$ Upwelling = 3) and average CO₂ fluxes (mmol m⁻² d⁻¹; M-W, Z = 2.0045, p = 0.071429, n Post-upwelling = 6, n Upwelling = 3). Specifically, during post-upwelling we found significantly higher: (I) Monthly average precipitation (746 \pm 214 vs 165 \pm 82 mm) due to the increased influence of the ITCZ and a moderate La Niña year; (II) Average sea surface temperature (27.5 \pm 0.4 °C vs. 26.5 \pm 0.2 ° C); and (III) Average pCO_{2w} and CO₂ Fluxes (567 \pm 64 μ atm vs. 450 \pm 55 µatm, and 0.2 \pm 0.09 mmol CO₂ m⁻² d⁻¹ vs. 0.1 \pm 0.06 mmol CO₂ m⁻² d⁻¹, respectively). Contrasting, in upwelling, we found a higher significant total pH mean (7.8697 vs 7.9686, respectively).



PCA test for stations and months considering the physicochemical variables SST, SSS, pCO₂, pH, DIC, and Chl-a. Note the grouping in the left quadrants for the months of February and March (upwelling, blue rectangle), from the upper right quadrant, May, June, and July (rainier season; post-upwelling, orange rectangle), highlighting the two contrasting seasons. The x axes explain the main variability 45.5% and the second axis y 28.1%. The colors represent the different sites and their corresponding sampling months.

3.1 Air-sea CO₂ exchange

During the moderate 2021-2022 La Niña event, surface waters around Gorgona displayed a near-neutral net CO2 flux (0.0105 ± 0.0001 mol C m⁻²) over the nine sampled months, with a bimodal pattern driven by upwelling and post-upwelling wet season (Figure 4). Throughout the upwelling season, cooler, saltier waters reached the surface (shallow thermocline), coinciding with the observed low pCO_{2w} values (below atmospheric levels, mean pCO_{2A} = 461 \pm 92.8 μ atm and negative Δ pCO₂, see Figures 4A-E), resulting in near-zero to weakly negative FCO2 (February-March, Figure 4F). This is additionally in line with elevated DIC and TA (Figures 4G, H). In contrast, during the post-upwelling period, the fluxes were slightly positive $(0.0093 \pm 0.0001 \text{ mol C m}^{-2})$ with an average pCO_{2w} of 567 \pm 97.5 μ atm (Figure 4D). Similarly, monthly fluxes also differed significantly between periods (Welch test, $F = 2.5 \times 10^{-4}$, p< 1 × 10⁻³⁰⁰; n = 9), peaking in June (2.5 mmol C m⁻² month⁻¹) and reaching a minimum in March (-0.1 mmol C m⁻² month⁻¹). Therefore, markedly higher fluxes were observed during the post-upwelling compared to the upwelling season when including the seven stations sampled per month (t = 4.91, critical t =2.00, p = 7.8×10^{-6} ; n = 21 vs. 39; Figure 4F).

Comparably, the average pCO_{2w} trend (Figure 4D) during the upwelling season evidences surface pCO_{2w} hovering moderately above atmospheric values in January (near 513 μ atm Figure 4D; atmospheric reference value ~418 μ atm, horizontal black line), but dips towards/just below atmospheric level by March (minimum average 397 μ atm). Correspondingly, a post-upwelling spike in pCO_{2w} increases values up to ~700 μ atm in May, around 1.7 times higher than atmospheric values, which drives a large positive ΔpCO_2 and outgassing (Figure 4E). Thereafter, pCO_{2w} slightly decreases until July, but remains well above atmospheric values (~580 – 590 μ atm).

The ΔpCO_2 values in eight of the nine months were above the atmospheric pCO_{2A} - (between 50 and 260 micro atmospheres). However, during the upwelling season, there is a reduction in pCO_{2w} , causing it to be less saturated than the pCO_2 of the surrounding atmosphere. Thus, March evidenced less pCO_2 in the water than in the air (negative ΔpCO_2 , Figure 4E) which is reflected with near-zero/negative FCO_2 (Figure 4F). Transition to the post-upwelling (higher rain and streamflow season; April-July) was also evident through the progressive increment in CO_2 peaking during May ($\Delta pCO_2 \gtrsim +250$ μ atm; more pCO_2 in the ocean than in the surrounding air) and then stabilizing, as reflected in the average CO_2 flux (Figure 4F).

3.2 Physical oceanographic conditions of sea surface temperature and salinity

The coolest temperatures were recorded during upwelling (\sim 26–26.5 °C). Rapid warming of the surface water was observed in April (\sim 28 °C) lasting until July (>27 °C). The shown warming is concurrent with the sharp rise in pCO_{2w} (Figures 4A, D). Average salinity was< 31 during the nine months, meanwhile, the highest

salinity was recorded during upwelling (31.2 in March). From April to July (post-upwelling months) a steady drop in salinity was measured, coinciding with the peak of precipitation/river discharge (Figure 2). Hence, markedly brackish water was observed (low-alkalinity via dilution), related to pCO_{2w} increase (Figures 4B, D, H).

3.3 Key parameters of the carbonate system: total alkalinity, pH_T , and dissolved inorganic carbon

The highest pH_T was measured in March (8.01), chemically consistent with reduced pCO_{2w} values and less riverine/ precipitation influence (Figure 4I). Then, pH_T began to decline during April and May (recorded a minimum of 7.81 in May) and stabilized after during June and July. Meanwhile, DIC start increasing between November and January (~1,700–1750 μ mol kg⁻¹) reaching its highest values in April (1,815 μ mol kg⁻¹) and May (~1800 μ mol kg⁻¹). After, there was a general decrease from May onward (~1,790–1,650 μ mol kg⁻¹ by July; Figure 4G).

The dominant DIC species, bicarbonate (HCO_3^-) , remained relatively stable from November to February (~1,550–1,600 µmol/kg, Figure 4J) then increased sharply from March-April (~1,720 µmol/kg) in line with the highest DIC/TA values. Thereafter, HCO_3^- decreased gradually during the post-upwelling season (May–July) mirroring the reduction in DIC/TA.

Carbonate ion (CO $_3^{2^-}$) values showed a clearer seasonal signal. They peaked during the upwelling months (January–March: ~170 and 180 µmol/kg, Figure 4K) in agreement with higher pH $_{\rm T}$ and $\Omega_{\rm AR}$ (Figures 4I, L). Afterwards, CO $_3^{2^-}$ concentrations decreased during the post-upwelling period, sharply decreasing in April to ~150 µmol/kg, then rebounding slightly during May to ~170 µmol/kg, and finally steadily decreasing to its minimum values from June to July (114–118 µmol/kg) coinciding with lower pH $_{\rm T}$, elevated Revelle Factor, and reduced $\Omega_{\rm AR}$.

3.4 Biological proxy signals

Monthly accumulated Chl-a (sum of seven stations) was relatively high during the sampling period (\sim 16–19 mg m⁻³, Figure 4M), with average Chl-a of 1.09 – 2.77 mg m⁻³ per sampled site (see Supplementary Figure 2). A marked increase from February to March was observed (16 – 19.4 mg m⁻³). Afterwards, Chl-a values remain high during May (17.2 mg m⁻³) until July with \sim 18 mg m⁻³ (Figure 4).

3.5 Key chemistry parameters of oceanic chemistry: Revelle Factor and omega aragonite

The Revelle Factor (RF, Figure 4N) and Ω -aragonite (Ω_{AR}) displayed an inverse relationship. The lowest RF values (9.9)

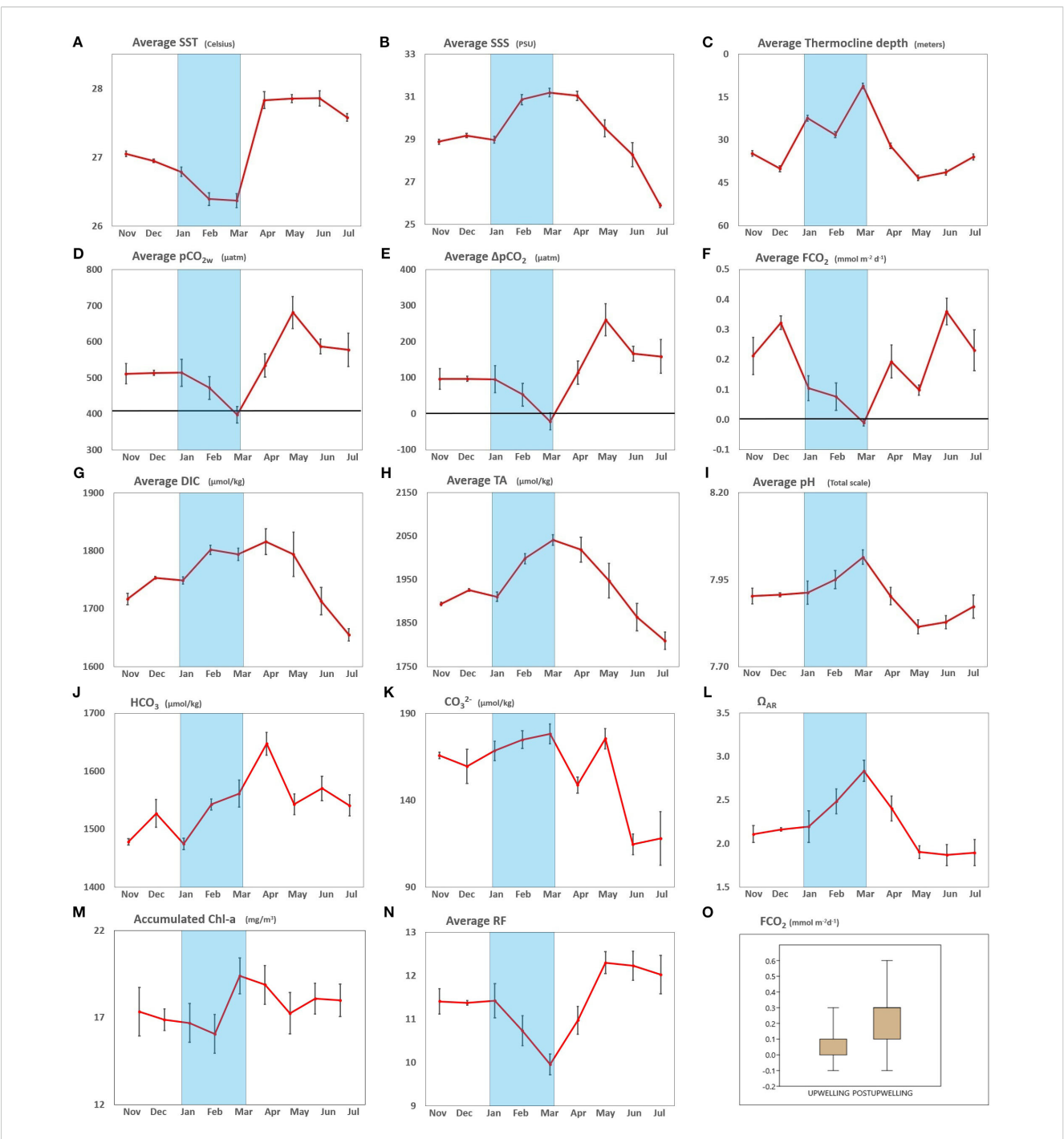


FIGURE 4 Monthly cycle of: (A) Average sea surface temperature (SST). (B) Average sea surface salinity (SSS). (C) Average thermocline depth (meters). (D) Average pCO_{2M} with average pCO_{2M} mark (418 μ patm) indicated with a black horizontal line. (E) Average ΔpCO_2 with zero delta mark indicated with a black horizontal line. (G) Average Dissolved Inorganic Carbon (DIC). (H) Average Total Alkalinity (TA). (I) Average pH in total scale. (J) Average bicarbonate (HCO3). (K) Average carbonate (CO32-). (L) Average Saturation state of aragonite (ΔpC). (M) Accumulated Chlorophyll concentration (Chl-a). (N) Average Revelle Factor. (O) Boxplot comparing FCO2 values between upwelling (January, February, March) and post-upwelling (November, December, April, May, June, July) evidencing statistical differences (T test, T = 4,908, Tc = 2.001, p = 7.80E-6, N = 21 vs 39, respectively). Monthly measurements around Gorgona near the surface (≤ 3 m), standard error is illustrated as a black vertical line on each data point. Note that ΔPC AR data starts above 1.2, indicating possible but suboptimal calcification throughout the sampled period.

occurred in March, coinciding with weakened or even collapsed stratification (Figure 4C), when Ω_{AR} reached its peak (2.8). In contrast, RF increased during the post-upwelling season, rising from April and reaching \geq 12 by July, concurrent with the lowest Ω_{AR} values (1.9), indicating suboptimal conditions for calcification. As expected, Ω_{AR} was inversely proportional to pH_T (Figures 4I, L), while RF varied inversely with SST.

3.6 Seasonal drivers of the carbonate system variability

Seasonal variability in dissolved inorganic carbon (DIC), its mixing component (DIC $_{\rm mix}$), and related drivers highlighted the coupled influence of physical circulation and biological activity (Figure 5). During the upwelling season, lower ΔDIC values coincided with reduced pCO $_{\rm 2w}$ and CO $_{\rm 2}$ fluxes, whereas in the post-upwelling season both DIC and pCO $_{\rm 2w}$ increased together with intensified Ekman transport and pumping (Figures 5B–D). Regional chlorophyll-a distributions also followed these seasonal shifts, with peaks during February–March and again in May–July (Figure 5C).

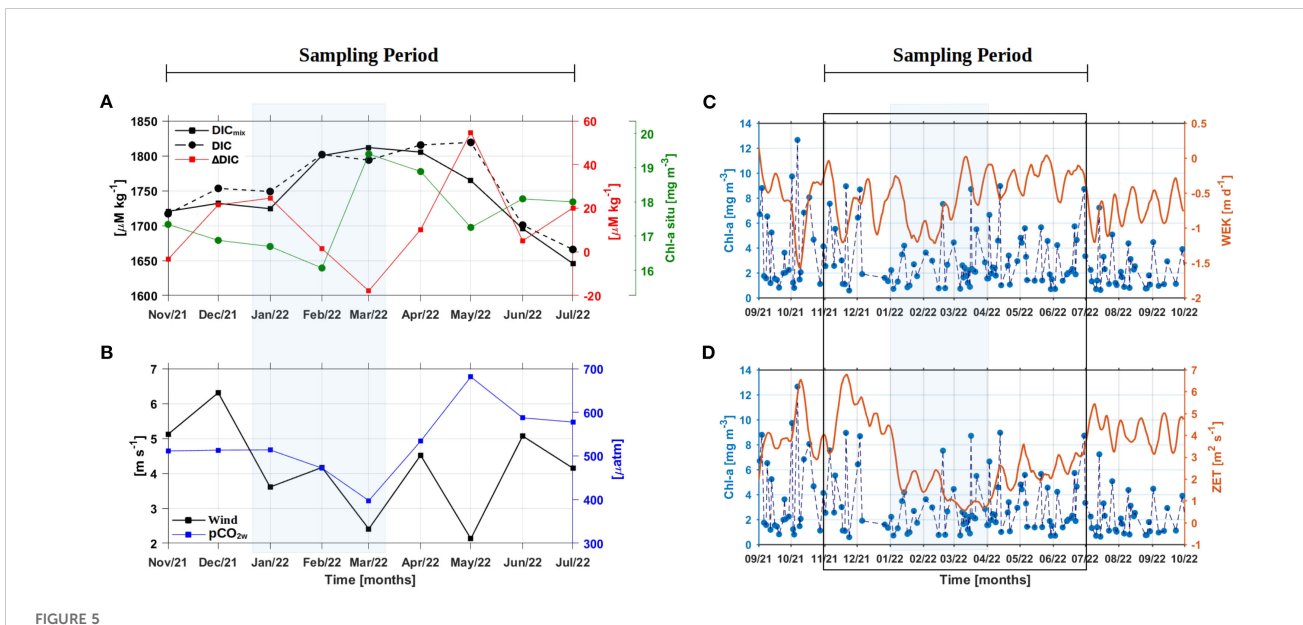
Complementary evidence from a temperature–salinity (T–S) diagram (Figure 6A) underscored the role of mixing in shaping carbonate chemistry. Mixing calculations indicated that up to ~79% of the observed DIC could be explained by conservative mixing of three endmembers, while the residual ~19% reflected non-conservative processes (Figure 6B). The correlation between Δ DIC and Δ O₂ (Figure 6C) suggested that aerobic

remineralization and nitrification were the dominant biological drivers of this residual variability. Physical processes dominated DIC variability, as indicated by the strong correlation between DICmix and DIC ($R^2=0.79$, Figure 6B). In contrast, respiration explained a smaller but measurable fraction of the variance ($\Delta \text{DIC}-\Delta \text{O}_2$, $R^2=0.19$; Figure 6C). Together, these results highlight that both physical and biological controls on DIC ultimately influenced its relationship with pCO_{2w}, consistent with the significant negative correlation observed between the two variables (Q=-0.71, p< 0.001, n = 60; Figures 4D, G).

4 Discussion

4.1 DIC dynamics

The physical mixing of the water mass contributes significantly to explaining the DIC values in the system (Figure 6A) as validated by the relationship between DIC_{mix} and DIC (Figure 6B; ~78% of variability) and the seasonal variability of WEK and ZET (Figures 5C, D). Therefore, DIC increased from November to May (Figure 5A) and then decreased from June to July. During La Niña 2021-2022, estuarine dynamics were strongly modulated by horizontal and vertical exchanges between marine and freshwater sources. High-frequency tides (up to 4 per day, with amplitudes of 5 m; Cauca tide table 2021–2022) mixed riverine and oceanic waters, while mesoscale eddies and Ekman-Zonal transport introduced deep offshore waters into the system (Corredor-Acosta et al., 2020; Figures 5C, D). Wind speed and direction generate local



Temporal variability of DIC, DIC_{mix}. DeltaDIC and accumulated *in situ* Chl-a values in **(A)**. Monthly average values of wind and pCO_{2w} of the *in situ* sampling stations in **(B)**. For comparison and higher resolution analysis, weekly data of regional satellite Chl-a data from the OC-CCI product (https://www.oceancolour.org/) was coupled with weekly Ekman pumping (WEK in **C**) and Zonal Ekman Transport values (ZET in **D**). Weekly wind fields for the above calculations were obtained from the CCMP Wind Vector Analysis Product (https://www.remss.com/measurements/ccmp/). Note that the left-panels consider the *in situ* sampling period between Nov/2021 to Jul/2022, while the right-panels consider a full year of variability including months before, during (black rectangular box), and after the sampling period (Sept/2021 to Sept/2022). Transparent blue rectangle indicates the upwelling period from January to March 2022.

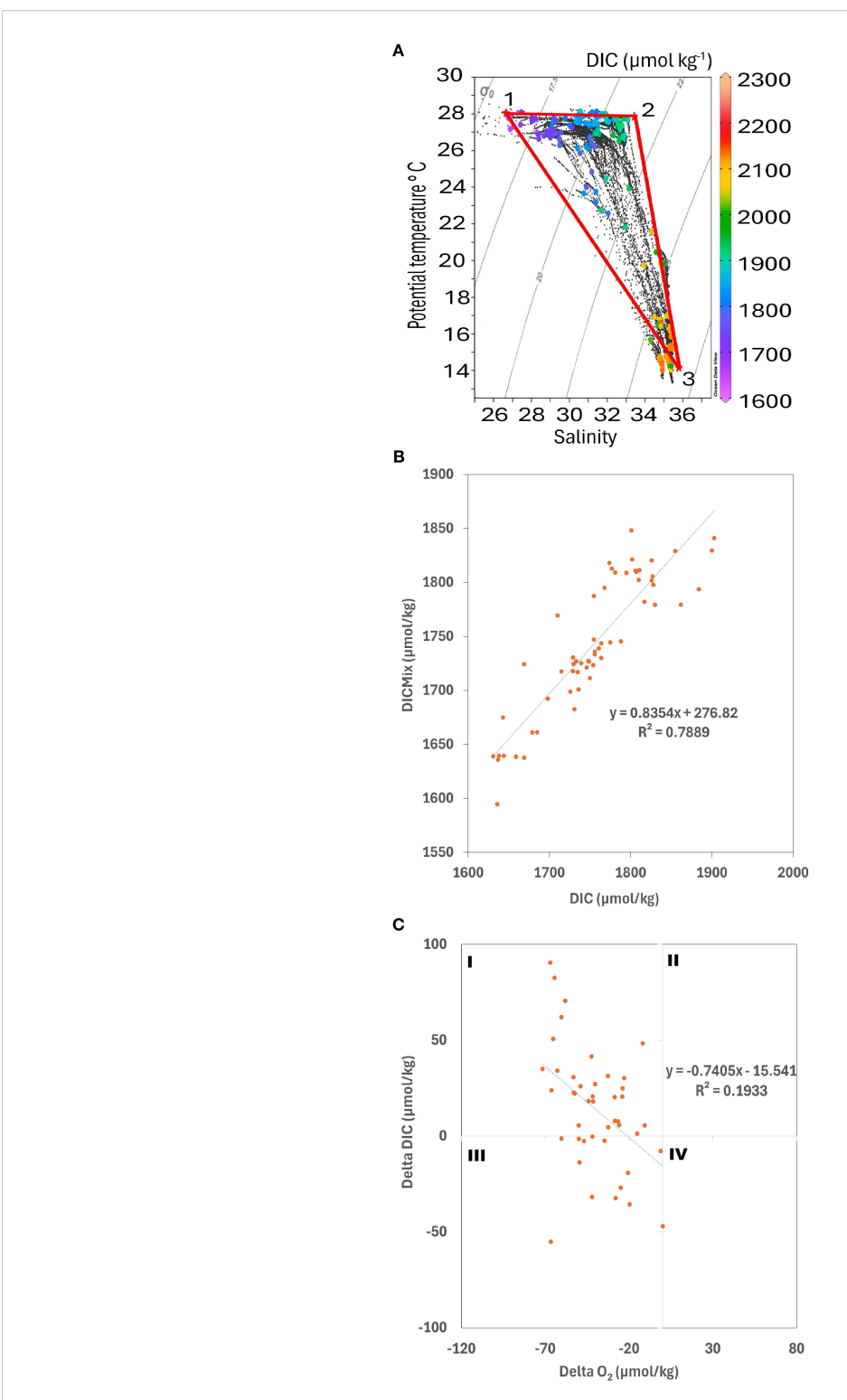


FIGURE 6 Temperature-salinity (T-S) diagram (A). Data points color-coded by dissolved inorganic carbon (DIC) concentration (μ mol kg⁻¹). The points represent observed oceanographic sampled depths throughout the year. The numbered labels (1-3) denote the end members of distinct water masses, with their respective salinity (S), potential temperature (T), and DIC values. The solid red lines connecting these end members outline the considered mixing triangles. Positive regression between DIC_{mix} and DIC (B). Physical process explains 78.8% of the DIC measured (DIC_{mix}). The remaining percentage is explained by biogeochemical processes (19%). Δ DIC (biological processes) and Δ O₂ (μ mol/kg) relationship (C; explaining 19%), where sampling points were mainly distributed within quadrants I and III (as shown in Kahl, 2018), suggesting aerobic remineralization and nitrification, respectively.

coastal currents, with north-south surface flow above the thermocline and south-north flow in subsurface waters (in situ observations); and upwelling and subsidence cycles (downwelling; Figures 5C, D) producing three water masses with different densities along the vertical profile (up to 80 m; see Figure 6A). Peaks in DIC between January and March coincided with intensified WEK and ZET which enhanced vertical injection of CO2 and TA rich subsurface waters, when freshwater dilution and stratification was weaker (lower relative rain and precipitation; Figures 2B, D). Even so, elevation of DIC values could also be due to a gradual increase of bicarbonate and carbonate in the system (Figures 4J, K), when acidic sub-superficial waters (Ω_{AR} values sometimes below 1.5, Preciado A., unpublished data) could dissolve the reef structure, bringing the increased DIC signal to the surface. From April to July, the relative decrease in DIC reflected dilution by enhanced river discharge and weaker zonal inputs. The residual variability (~19%) was linked to respiration and remineralization, as evidenced by the correlation between ΔDIC and ΔO_2 where DIC increased but O2 decreased (Figure 6C; O2 levels reached 60 µmol/ kg) and pCO_{2w} values were elevated. However, this respiration hypothesis requires further studies in the study site, to understand its contribution in DIC variability.

4.2 Seasonal FCO₂ variability

The seasonal variability of FCO₂ in Gorgona during the study period resulted from the system shifting from post-upwelling, dominated by southerly trade winds, higher precipitation and river dominated system to upwelling, dominated by northern winds, less precipitation, and lower river discharge, and then back to post-upwelling season. During post-upwelling, a slight positive increase in FCO2 is related to the extensive plume of water from coastal rivers (Figure 2) originating from a 44% increase in river flow during the study period (e.g., the Guapi River with 103 m³ s⁻¹; Figure 2D), this plume extended for more than 60 km from the coast (as observed by floating logs on the field), forming a large estuary with an average salinity of 29.51 units (SD \pm 1.56). Thus, following the definitions of Dai et al. (2013) and McKee et al. (2004), our study area can be classified as a system dominated by riverine inputs. During the post-upwelling season, pCO_{2W} values were relatively high (Figure 4D), ranging from 378 to 839 µatm (average 567 µatm), peaking in May, in line with high SST (Figure 4A), and ΔpCO₂ ranging from 47 μatm to 418 μatm. Our results agree with Ricaurte-Villota et al. (2025), where rivers via remineralization could explain the high pCO_{2w} values during moderate La Niña years (see Figure 6C). But also, the increased freshwater discharge could also diminish CO2 fluxes, simultaneously, under La Niña (Reimer et al., 2013; Ricaurte-Villota et al., 2025), via nutrient excess and phytoplankton bloom. During upwelling season, the average water temperature decreased to 26.53 °C, but the average salinity remained below 30, confirming the rivers influence on surface waters. Likewise, the pCO_{2W} was relatively lower, ranging from 316 to 626 µatm (average 461 ± 92 uatm), with minimum values in March, coinciding with the lowest

surface temperature (26.11 °C) and highest salinity (28.39). During this period, FCO₂ reached negative or near neutral values (between 0.3 and -0.1 mmol m⁻² d⁻¹), with similarly low ΔpCO₂ values, ranging from -101 µatm to 93 µatm. Despite theory indicating that upwelling during a moderate La Niña should increase the CO2 flux to the atmosphere (Kim et al., 2017), this was not observed in our study site. Similar dynamics i.e., low or negative net fluxes despite upwelling have been reported in tropical estuarine systems where upwelled DIC is rapidly consumed by phytoplankton blooms which counterbalance the physical delivery of dissolved carbon (e.g., Vargas et al., 2007; Bouillon, 2011; Giraldo et al., 2011). Monthly patterns and flux directions were preserved when calculated using the propagated pCO_{2w} error, including the neutral/slight sink observed in March, with only December and June showing greater variability. Net flux differences over the nine-month period remained negligible (original net flux = 0.0105 mol C m⁻², positive error net flux = 0.0133 mol C m⁻², negative error net flux = $0.0077 \text{ mol C m}^{-2}$) indicating a net total difference of $\pm 0.0028 \text{ mol C}$ m⁻², confirming the robustness of our results.

4.3 Temporal pCO $_{2W}$ variability and key associated variables: salinity, temperature, dissolved inorganic carbon and ΔO_2

The temporal variability of pCO_{2W} was shaped by the combined effects of salinity, temperature, DIC, and ΔO₂ variables were correlated with pCO_{2W} values. Salinity showed the strongest and most significant correlation with pCO_{2w} (Q = -0.96; p = 1.77E⁻³⁶, n = 60) reflecting the strong influence of river discharge and freshwater dilution, particularly during post-upwelling months, which differs from many oceanic regions where temperature is typically the main driver of FCO₂ variability (Séférian et al., 2013). Ekman-driven processes contributed to FCO₂ variability by vertical mixing processes (upwelling, downwelling; Figure 5C) that reduce salinity up to 40-60m, modifying the depth of the mixed layer over time. Sea surface temperatures recorded at the study site were relatively high (26.1-28.1 °C), as foreseen at equatorial latitudes, due to maximum solar insolation (Saraswat, 2011). On the other hand, sea surface temperature also correlated positively with pCO_{2w} (Spearman Q = 0.42313, p = 0.0007, n = 61; Figure 4A), in line with previous findings by Zhai et al. (2005), who reported higher pCO_{2w} values during warmer seasons. During the post-upwelling, the increase in SST from April to June aligned with increases in pCO_{2W}, Δ pCO₂, and FCO₂. As a result, the observed trend is consistent with the thermodynamic relationships between temperature and CO₂ solubility (Johnson et al., 2010), even though sea surface temperature alone did not fully explain the FCO₂ variability. Furthermore, we assessed the relative influence of salinity and temperature to pCO_{2W} by performing a sensitivity test which fixed one of the variables (salinity or temperature) while allowing the other to vary in the CO2SYS, recalculating pCO_{2w}. This approach allowed us to isolate the individual effect of each parameter (see Supplementary Figure 1). Results showed that salinity explained a larger proportion of the variance -

particularly in June and July when riverine CO2 inputs were strongest, supporting the findings of Ricaurte-Villota et al. (2025) who also observed that river influence on salinity in the Colombian Caribbean exerts a greater control on pCO_{2w} than temperature. The lower salinity observed in June (post-upwelling) was associated with higher pCO_{2w} values, consistent with dilution by freshwater input and potential organic and inorganic matter increase from riverine mangrove sources (Palacios Peñaranda et al., 2019). The observed negative relationship between DIC and pCO_{2W} reflects the seasonal interplay of physical and biological processes at Gorgona. During upwelling, physical mixing and water mass advection introduced CO2-rich subsurface waters, but biological drawdown suppressed pCO_{2w} provided by the sea and rivers. On the contrary, during the post-upwelling phase, the DIC increases and then decreases, due to the antagonistic relationship between the mixture (ZET, WEK; Figure 5) that, like respiration processes (oxygen reduction; Figure 6), provide pCO_{2w} (and DIC), and the photosynthetic activity, which consumes it or the excess of fresh water that dilutes the DIC (Figure 4).

Overall, the patterns in Figure 6 suggest that physical mixing and dilution were the primary controls of DIC variability, consistent with estuarine systems where hydrodynamic forcing often dominates carbon system fluctuations (Clark et al., 2022). Nevertheless, biological processes such as respiration and photosynthesis clearly modulated the signal, producing seasonal configurations of DIC-pCO_{2W} values that reflect the co-occurrence of both physical and biogeochemical drivers. Similar interactions have been reported in estuarine environments by Ahad et al. (2008) and Quiñones-Rivera et al. (2022), where strong physical control is complemented by meaningful, localized biological contributions. As anticipated, pH's relationship to pCO_{2w} was inverse (Peng et al., 2013; Hans-Rolf and Fritz, 2023; Ramaekers et al., 2023), and direct with Ω_{AR} (See Figure 4I), which is similar to the relationship described by Feely et al. (2009), in our case also in agreement with the highest salinity values. In addition, high pH_T values during March were coupled with consumption of CO₂ by phytoplankton (lowered pCO_{2w}), and higher buffer capacity in the system (high TA; Figure 4), which is similar to cases reported by Cai et al. (2011) and Macdonald et al. (2009) in coastal and estuarine systems (low SSS), despite relatively high DIC values. This condition favors coral reef or marine organisms' calcification, although the Ω_{AR} remained below 3, suggesting thermodynamically possible, yet suboptimal conditions (Ries et al., 2009). On the other hand, pH_T decreased during post-upwelling, to its minimum values (May; 7.81), as did TA (~1800 μmol kg⁻¹, Refer to Figure 4H), when the pCO_{2w} was at its maximum, thereby lowering the Ω_{AR} below 2.

4.4 Biological processes

The apparent suppression of CO₂ fluxes under upwelling conditions contradicted expectations from classical upwelling theory (e.g., Kim et al., 2017), which generally predicts enhanced CO₂ outgassing as deeper, carbon-rich waters reach the surface. Instead, rapid phytoplankton uptake offset the physical inputs

(rivers, subsurface water, advection, atmosphere, and other sources). Evidence for this mechanism comes from strongly negative ΔDIC values in February and March (Figure 6D), indicating intense CO_2 consumption, and from the inverse relationship between surface $\text{pCO}_{2\text{w}}$ and cumulative Chl-a concentrations (Figures 4D, M; Figure 5A). This agrees with the findings of Corredor-Acosta et al. (2020) who reported peak productivity around Gorgona during March, based on multiannual satellite observations. Both their long-term satellite information and our average and accumulated Chl-a data (Figure 4M) confirm that the coastal waters near Gorgona sustain relatively high phytoplankton biomass throughout the year, with average concentrations exceeding 2.45 mg m⁻³ in both seasons, and accumulated values surpassing 16 mg m⁻³ (Figure 4M; Supplementary Figure 2).

According to Corredor-Acosta et al. (2020) the sustained Chl-a signal on the Colombian Pacific coast is modulated by rising waters along the Panama Bight during the upwelling season and river discharges (see also Rodríguez-Rubio et al., 2003; Devis-Morales et al., 2008; Giraldo et al., 2008; 2008; 2011). Therefore, the productivity observed in Gorgona is attributed to the constant input of nutrients (Giraldo et al., 2011), coming from both, subsurface waters and the nearby Patía-Sanquianga deltaic complex (~50 km), which contributes total suspended solids (23.2 mg L⁻¹), nitrates (33.55 μg L⁻¹), and phosphates (<2 μg L⁻¹; Giraldo et al., 2011). These inputs, according to INVEMAR (2019-2022) result in high Chl-a concentrations near the coast (~0.9 mg m⁻³) compared to areas farther from the island (~0.3 mg m⁻³). Additionally, the coastal phytoplankton around Gorgona is dominated by large diatoms and dinoflagellates which support a zooplankton biomass up to seven times greater (89 g/100 m³) than the regional average for the Colombian Pacific (12 g/100 m³; Murcia Riaño and Giraldo López, 2007; Giraldo et al., 2011). Therefore, zooplankton also facilitates carbon export through marine snow, contributing to remineralization in the water column and up approximately 90-100 m depth (Alldredge, 1984; Vargas et al., 2007) which further aids in pCO_{2w} modulation at the surface (WEK, Figure 5C). The persistence of such high productivity effectively modulates surface pCO_{2w} by enhancing phytoplanktonic CO2 uptake, thereby reducing the magnitude of air-sea fluxes. Without this sustained biological activity, surface waters around Gorgona would likely accumulate greater CO2 excesses and display substantially higher efflux to the atmosphere during La Niña years.

4.5 Potential drivers for low CO₂ flux

The near-neutral to slightly positive CO_2 fluxes observed around Gorgona can be understood as the outcome of several interacting climatic–oceanographic processes. As shown, the system displays marked seasonal variability, yet overall fluxes remained low to neutral compared with other tropical Pacific or estuarine sites. Three main drivers appear to regulate this behavior: wind-driven exchange, vertical stratification, and the buffering capacity of surface waters.

Wind speeds during the study period were consistently low (mean<5 m s⁻¹; range: 2.1–6.4 m s⁻¹; Figure 5), which limited the efficiency of gas transfer. Since air–sea CO_2 fluxes are jointly governed by wind speed and the air–sea CO_2 partial pressure gradient (ΔpCO_2), the absence of high-wind events (>10 m s⁻¹; Prytherch et al., 2010) meant that surface–atmosphere exchange remained weak throughout most of the year. Even when ΔpCO_2 values were favorable for outgassing, limited wind-driven turbulence constrained fluxes to the atmosphere.

Vertical stratification further reinforced this suppression. The water column at Gorgona remained strongly stratified for most of the year, with the thermocline-halocline-pycnocline complex typically lying between 11 and 40 m depth (Figure 4C). This effectively isolated subsurface CO₂-enriched waters from the surface, preventing their sustained transfer into the mixed layer. Only in March, during the shoaling of the thermocline (to ~11 m), did subsurface waters briefly reach the surface, temporarily breaking stratification. Yet even under these conditions, fluxes remained near-neutral rather than shifting strongly positive.

This apparent contradiction can be explained by the buffering capacity of surface waters. Revelle Factor (RF) values were lowest during upwelling (January–March; Figure 4N), indicating a high resistance of surface waters to changes in pCO_{2W} despite inputs of dissolved inorganic carbon (DIC) from below. As a result, increases in subsurface DIC did not translate into proportional rises in surface pCO_{2W}, thus preventing strong efflux. By contrast, RF increased during the post-upwelling period (May–July; Figure 4N), when surface waters became more sensitive to DIC changes. Nevertheless, stratification was then strongest, reducing the vertical supply of CO₂-rich subsurface waters and limiting fluxes.

Taken together, these mechanisms explain why Gorgona exhibited suppressed CO₂ efflux during both upwelling and post-upwelling conditions. Wind limitation constrained the physical transfer of CO₂, stratification acted as a barrier separating sources from the surface, and buffering capacity modulated the extent to which subsurface DIC inputs could alter surface pCO_{2W}. This combination is consistent with earlier findings in the Colombian Caribbean (Reimer et al., 2013; Ricaurte-Villota et al., 2025), where La Niña-driven stratification similarly reduced CO₂ outgassing. At Gorgona, therefore, the interplay of seasonal stratification and surface carbonate chemistry set the stage for fluxes that remained near-neutral, even under physical conditions that would normally favor enhanced CO₂ release.

4.6 Gorgona's CO₂ fluxes in the context of global and regional estimates

To enable comparison of our nine-month flux record with annual estimates reported in literature, we estimated the three missing post-upwelling months (August to October 2020) in order to derive a potential annual flux. This approximation was based on our *in situ* measurements from six post-upwelling months that correspond to the rainy (wetter) season, a period which also encompasses the missing months. From these six months, we

calculated a mean monthly flux of 0.00024 \pm 0.0001 mol C m². Using this value, we estimated the flux for the three missing months (0.0007 mol C m²; net positive flux) and added it to the nine-month total (0.01049 \pm 0.000148 mol C m²) yielding a potential annual flux of 0.0112 \pm 0.00015 mol C m² yr¹. Interpolation of missing FCO₂ data has been applied previously (e.g., Kahl, 2018). Nevertheless, we emphasize that the estimated three-month flux is a hypothetical approximation intended only for comparison purposes, and should be validated with additional *in situ* measurements.

This approach revealed a neutral to weakly positive net air-sea CO_2 flux at Gorgona Island (FCO₂ = 0.0112 \pm 0.00015 mol C m⁻² yr⁻¹; ~0.031 mmol C m⁻² d⁻¹) being an order of magnitude lower than those reported by Dai et al. (2022) for non-ENSO years (0.8–1.0 mol C m⁻² yr⁻¹), and close to the lower limit of the global range reported by Wong et al. (2022) for surface ocean carbon fluxes (0–1.5 mol C m⁻² yr⁻¹); highlighting potential regional divergence from global modeling outputs (Table 1).

The Gorgona fluxes were also markedly lower than those observed in other tropical and coastal systems. For instance, at similar equatorial latitudes (~3°N), Jersild et al. (2017) and Landschützer et al. (2022) reported fluxes exceeding 0.3 ± 0.1 mol C m⁻² yr⁻¹ during moderate La Niña conditions. Pacific Ocean continental shelves exhibit values between 0.2 and 0.35 mol C m⁻² yr⁻¹ (Jersild et al., 2017; Vaittinada Ayar et al., 2022), while the North Pacific shelf, even under non-ENSO conditions, registers around 0.043 mol C m⁻² yr⁻¹ (Reimer et al., 2013). These regional differences suggest that local environmental controls strongly limit the air-sea CO2 exchange in the Eastern Tropical Pacific, particularly near Gorgona. Consistent with this interpretation, Ricaurte-Villota et al. (2025) documented similarly low to nearneutral fluxes in the Colombian Caribbean under La Niña conditions, attributing them to high rainfall, enhanced stratification, and strong biological uptake. These drivers mirror those identified in our study, reinforcing the idea that La Niña exerts a suppressive effect on CO2 release in this region. Comparable mechanisms have also been described in Arctic continental shelves, where freshwater inputs from rivers and ice melts (together with seasonal ice coverage) enhanced stratification, restricting gas exchange and contributing to low or near-neutral fluxes (Else et al., 2013; Miller et al., 2019; Mu et al., 2020).

Furthermore, comparison with other tropical systems reinforces our findings. Similar low or near-neutral fluxes have been reported in Costa Rica's Gulf of Nicoya (Pfeil et al., 2013) and other areas of the Eastern Tropical Pacific (Laurelle et al., 2013).

Estuarine systems by contrast, tend to show higher fluxes and yearly variability (Chen et al., 2013). For example, the Matla estuary in India exhibits high annual fluxes of 2.3 mol C m⁻² yr⁻¹ (Akhand et al., 2016) over 10 times greater than the estimated CO₂ flux around Gorgona, and the Patos Lagoon in Brazil ranges from -13.9 to 19.7 mol C m⁻² yr⁻¹ attributed to changes in freshwater input and phytoplankton activity (Albuquerque et al., 2022). Meanwhile Asian tropical estuaries average around 8.1 mol C m⁻² yr⁻¹ (Chen et al., 2013) which are also substantially higher than our estimated yearly fluxes. However, comparable near-neutral fluxes were reported in the Arafura and Red Seas under similar La Niña conditions (Hydes et al., 2012).

TABLE 1 CO₂ fluxes between air and sea in different geographic areas.

Location	Long.	Lat.	Continent	CO ₂ Flux (mol C m ⁻² yr ⁻¹)	ENSO state	Reference
Southeast Asia	115°E	2.2°S	AS	0.86 ± 17	Moderate Niño	Laurelle et al. (2013)
Northern Australia	125°E	8.9°S	OC	0.11 ± 15.7	Moderate Niño	Laurelle et al. (2013)
Caribbean Sea	75°W	14.5°N	SA	0.66 ± 4.5	Moderate Niño	Laurelle et al. (2013)
Tropical Ocean	90°E – 90°W	20°S – 20°N	NA/SA	2.4 ± 0.05	Moderate Niño	Laurelle et al. (2013)
Matla Estuary	88°E	20°N	AS	2.3 + 0.5	Strong Niño	Akhand et al. (2016)
Patos Lagoon	52.5°W	6°N	SA	-13.9 – 19.7	Moderate Niña	Albuquerque et al. (2022)
Omani coast	59°E	20°N	AS	-0.9 ± 0.03	Strong Niña	Millero et al. (1998)
South China Sea (North)	116°E	22°N	AS	0.86 ± 0.04	Weak Niño	Zhai et al. (2005)
South China Sea (North)	116°E	22°N	AS	0.4 ± 0.2	Weak Niña	Li et al. (2022b)
Eastern Equatorial Pacific Ocean	90°W - 165°E	5°N - 10°S	NA/SA - OC	2 ± 1	Weak Niña	Cosca et al. (2003)
Equatorial Pacific Ocean	270°E	3°N	SA	0.20 ± 0.02	Moderate Niña	Vaittinada Ayar et al. (2022)
Red Sea	42.8°E	13.4°N	AS/AF	0.01 ± 0.001	Moderate Niña	Hydes et al. (2012)
Gulf of Nicoya	-84.9°W	9.6°N	CA	-0.02 ± 0.001	NA	Palacios Moreno and Pinto Tovar (1992) (SOCAT)
Arafura Sea	136.3°E	-9.9°S	OC	-0.01 ± 0.001	Moderate Niña	Hydes et al. (2012)
Amazon River plume	-52.5°W	6°N	SA	-12.78 ± 0.02	Weak Niña	Kortzinger (2003)
Equatorial Pacific	125°W	3°N	SA	0.3 ± 0.1	Moderate Niña	Landschützer et al. (2022)
Equatorial Pacific	125°W	3°N	SA	1.5 ± 0.03	Strong Niño	Cosca et al. (2003)
Tropical Eastern Pacific	-81°W	4.7°N	SA	-0.05 ± 0.01	NA	Laurelle et al. (2013)
Subarctic Pacific	145°E	50°N	AN	0.7 ± 0.5	Moderate Niño	Wang et al. (2018)
North Pacific Shelf	118°W	28°N	NA	0.35 ± 0.07	Weak Niña	Jersild et al. (2017)
North Pacific Shelf	117°W	31°N	NA	0.043 ± 0.01	NA	Reimer et al. (2013)
Colombian Atlantic	77°W	10°N	SA	0.25 ± 0.05	Weak Niña	Vaittinada Ayar et al. (2022)
Caribbean Coast	74°W	11°N	SA	0.02 ± 0.01	Moderate Niña	Ricaurte-Villota et al. (2025)
Equatorial Pacific Coast	78°W	3°N	SA	0.0112 ± 0.0001	Moderate Niña	This study (2021-2022)

It is important to note the flux difference when comparing systems at low latitudes, even during ENSO years. The similarity of the flux in the Colombian Pacific with tropical systems in the western Pacific Ocean is observed, even if they are located in Asia or Oceania. The abbreviations for continents are: AS, Asia; OC, Oceania; SA, South America; NA, North America; AF, Africa; CA, Central America; AN, Antarctica; EN, El Niño and LN, La Niña. The ENSO state is based on the ONI index from NOAA. Note that the value for this study is the predicted yearly flux for easier literature comparison.

Although global models (*e.g.*, Dai et al., 2022) and some regional studies do not explicitly separate ENSO phases, this distinction is essential for accurately characterizing flux dynamics in equatorial regions such as Gorgona. Prior literature indicates that La Niña conditions can reduce FCO₂ by 0.2–0.4 mol C m⁻² yr⁻¹ in the Pacific region, compared to El Niño or neutral years, aligning with the low values observed in this study (Chavez et al., 1999; Landschützer et al., 2016; McKinley et al., 2020; Park et al., 2010).

Our findings challenge the assumption that upwelling-dominated systems and estuarine environment are high CO_2

emitters, especially under La Niña conditions. Since in our tropical coastal area FCO_2 is sensitive to atmospheric conditions (wind velocity, precipitation, solar radiation), freshwater discharge, physical dynamic (vertical-horizontal water movement), vertical stratification, upwelling events, carbonate chemistry and biological uptake. Future research should incorporate higher-resolution temporal data, uncertainty analyses in ΔpCO_2 , and ENSO-phase-specific studies (and neutral/non-ENSO years) to improve carbon flux estimates in this and similar tropical estuarine systems.

4.7 Methodological considerations and recommendations

Our study did not include measurements of δ^{13} C-DIC, which limits our ability to trace the biogeochemical sources and transformations of dissolved inorganic carbon. This isotopic parameter is a powerful tool for distinguishing between marine, terrestrial, and anthropogenic carbon inputs, and for assessing the extent of biological activity and remineralization. Its absence constrains our interpretation of carbon cycling dynamics, particularly under varying ENSO conditions. We suggest that future sampling campaigns incorporate δ¹³C-DIC analysis to enhance source attribution and improve the mechanistic understanding of CO2 flux variability in coastal upwelling systems. Additionally, we did not directly measure nutrients, which limits our ability to consider them in the CO2SYS calculations, specifically those which are proton acceptors (e.g. phosphates, silicates, ammonia), which can have effects on the computation of certain carbonate system parameters under high nutrient loads. We recommend that future sampling efforts incorporate nutrient measurements for improved flux and carbonate system calculations.

It is important to consider methodological differences when comparing with other studies. Although references such as Feely et al. (2004, 2006) and Hydes et al. (2012) offer context, disparities in sampling protocols, spatial resolution, and ecosystem type limit the scope of direct comparison. Finally, we recommend a long-term monitoring program taking water samples to estimate in the lab the couple DIC/TA, this will allow to compare the CO₂ flux variability between ENSO events and neutral conditions. An inexpensive discrete sampling based on our experience for Gorgona National Park could be to take water samples for 2–4 contrasting months.

5 Conclusions

The estimated air-sea CO_2 flux at Gorgona Island (near 3°N in the Eastern Equatorial Pacific) was close to neutral (0.0104 mol C m⁻²) during the nine sampled months under La Niña conditions. Gorgona displayed a bimodal regime: (I) a predominantly post-upwelling system for six months, characterized by slightly positive to near-neutral fluxes, augmented river discharge and rainfall, elevated sea surface temperatures (>27.4 °C), and high pCO_{2W} (567 μ atm in average); and (II) three months of upwelling, with neutral or weakly negative fluxes (-0.1 \pm 0.07 g C m⁻² day⁻¹), associated with CO₂ rich subsurface waters (nutrient rich) and phytoplankton uptake (minimum values of DeltaDIC aligned with the Chl-a maximum).

Although subsurface waters and coastal rivers deliver CO₂ to the surface, the intense and persistent stratification from low TA/DIC freshwater (high Revelle factor values; stratification starting at 10 to 45 m), reinforced by warmer surface waters, and freshwater downwelling, effectively limits CO₂ venting to the atmosphere. The estimated air-sea CO₂ flux at Gorgona Island aligns with global estimates proposed by Wong et al. (2022). Still is lower than those

predicted by the model of Dai et al. (2022), suggesting the influence of local biogeochemical processes. In summary, under La Niña conditions, characterized by rainfall and river runoff (mean SSS = 29.5 ± 1.5) the combined effects of low wind speeds (<5 m s⁻¹), vertical stratification, and the biological activity appear to explain the net neutral balance in the air-sea CO_2 flux in this region. This study highlights the importance of integrating local physical and biological coastal processes (hydrography) when estimating region-specific CO_2 fluxes (in both magnitude and direction); additionally, long temporal *in situ* measurements under ENSO events such as El Niño and Neutral conditions are needed to compare with La Niña FCO₂ findings.

Nevertheless, the overall trend of low fluxes during La Niña, as shown across tropical estuaries and coastal systems, supports the hypothesis that this event suppresses CO₂ efflux through enhanced freshwater delivery and weakened ocean-atmosphere coupling. However, the hypothesis of high positive fluxes during El Niño or neutral years, when rainfall and upwelling are reduced at Gorgona, needs further investigation through seasonal and interannual monitoring campaigns including physical and biogeochemical variables.

Data availability statement

The datasets generated for this study can be found in the NOAA - National Centers for Environmental Information (NCEI; Accession Number 0300558). (NCEI; URL, https://www.ncei.noaa.gov/data/oceans/ncei/ocads/metadata/0300558.html).

Author contributions

SG: Writing – original draft, Formal analysis, Data curation, Writing – review & editing, Visualization, Software, Investigation, Validation, Methodology. AA: Conceptualization, Validation, Data curation, Supervision, Methodology, Project administration, Investigation, Resources, Writing – review & editing, Funding acquisition, Visualization, Formal analysis. AM: Methodology, Investigation, Visualization, Writing – review & editing. AG: Investigation, Data curation, Methodology, Writing – review & editing. AC-A: Conceptualization, Visualization, Writing – review & editing, Formal analysis. JH-A: Conceptualization, Writing – review & editing, Visualization. LC: Writing – review & editing, Validation, Methodology, Formal analysis, Visualization. LK: Visualization, Methodology, Formal analysis, Writing – review & editing. DR-P: Writing – review & editing, Supervision, Validation, Methodology.

Funding

The author(s) declare financial support was received for the research and/or publication of this article. The Principal Investigator (PI), AA, acknowledges receiving financial support for various research activities, including the purchase of

equipment, acquisition of laboratory and field materials, and funding for field trips. Additionally, these funds were used to establish and equip a laboratory at the Pontificia Universidad Javeriana. Partial resources from the same fund were also allocated to cover the publication costs of this article (ID 21346). This research was funded by the National Geographic Explorer program through the project titled "Ocean Acidification Vulnerability in Colombia: First Monitoring Program in the Tropical Pacific" (Grant No. NGS-64756R-19), with additional COVID-19 grant support (Grant No. NGS-81727R-20). Further funding was provided by the Pontificia Universidad Javeriana under the project "Monitoreo de acidificación marina en el Pacífico colombiano" (Project ID: 120132C0401200, No. 20019; Grant ID 21347).

Acknowledgments

The Ocean Foundation donated the GOA-ON in a Box kit, OA training, and grant support for equipment maintenance under the Memorandum of Understanding between Pontificia Universidad Javeriana and The Ocean Foundation ("TOF"). This research is part of the collaboration with the International COCAS project (2021-2030), Ocean Decade-United Nations (Leader Diana Ruiz Pino and Alban Lazar) https://oceandecade.org/fr/actions/coastalobservatory-for-climate-co2-and-acidification-for-the globalsouth-society-cocas/. Dra. Andrea Corredor-Acosta thanks FONDECYT Postdoctoral Project No. 3230740 granted by the Chilean Agency for Research and Development (ANID). We also thank Parques Nacionales Naturales de Colombia - Gorgona for their logistical support at Gorgona (Christian Díaz - research head & Monitoring of the Gorgona park), accommodation and boat, and the research permit No. 004 de 2020 - file number: OTRP 004-2020. To Camilo, Freddy, and Jaime for their help in the Ocean Acidification laboratory. To Juan Felipe Cifuentes for his field assistance (monitoring) and also to Gabriela Cervantes Diaz for her help in the laboratory analysis at the UABC. Thanks to Dr. Alan Giraldo of Universidad del Valle for funding research interns Cristian Claros, Sebastián Ortiz, and Natalia Londoño, who collaborated with us in the field sampling. We thank Camilo Rodríguez and Enrique Herman for their help during the long days of boat sampling and for hosting us in their home during our stay at Guapi. Finally, a huge thanks to my friends, Hugo Barata, Catalina Infante, Iván Gonzales, Vinny Preiss, and my family, Mónica Duque, Juan Pablo Gutiérrez, and Emma Gutiérrez for their never-ending support, without which this research would not have been possible.

Conflict of interest

The authors declare that the research was conducted in the absence of any commercial or financial relationships that could be construed as a potential conflict of interest.

Generative AI statement

The author(s) declare that no Generative AI was used in the creation of this manuscript.

Any alternative text (alt text) provided alongside figures in this article has been generated by Frontiers with the support of artificial intelligence and reasonable efforts have been made to ensure accuracy, including review by the authors wherever possible. If you identify any issues, please contact us.

Publisher's note

All claims expressed in this article are solely those of the authors and do not necessarily represent those of their affiliated organizations, or those of the publisher, the editors and the reviewers. Any product that may be evaluated in this article, or claim that may be made by its manufacturer, is not guaranteed or endorsed by the publisher.

Supplementary material

The Supplementary Material for this article can be found online at: https://www.frontiersin.org/articles/10.3389/fmars.2025.1633653/full#supplementary-material

References

Ahad, J. M. E., Barth, J. A. C., Ganeshram, R. S., Spencer, R. G. M., and Uher, G. (2008). Controls on carbon cycling in two contrasting temperate zone estuaries: The Tyne and Tweed, UK. *Estuarine. Coast. Shelf. Sci* 78, 685–693. doi: 10.1016/j.ecss.2008.02.006

Akhand, A., Chanda, A., Manna, S., Das, S., Hazra, S., Roy, R., et al. (2016). A comparison of $\rm CO_2$ dynamics and air-water fluxes in a river-dominated estuary and a mangrove-dominated marine estuary. *Geophys. Res. Lett.* 43. doi: 10.1002/2016gl070716

Albuquerque, C., Kerr, R., Monteiro, T., MaChado, E.da C., Carvalho, A. da C.d., and Mendes, C. R. B. (2022). Water-air exchanges in the lower estuary of the patos lagoon: seasonal variability, drivers, and sources of CO₂. doi: 10.21203/rs.3.rs-1336400/v1

Alldredge, A. L. (1984). "The quantitative significance of gelatinous zooplankton as pelagic consumers," In: M. J. R. Fasham (eds) *Flows of Energy and Materials in Marine Ecosystems* (Boston, MA: Springer US), 407–433. doi: 10.1007/978-1-4757-0387-0_16

Amaya, C. A. A. (2024). "Las corrientes superficiales en la cuenca de Colombia observadas con boyas de deriva," in *Revisa de la Academia Colombiana de Ciencias Exactas, Físicas y Naturales*, vol. 25. Bogotá, Colombia: Academia Colombiana de Ciencias Exactas, Físicas y Naturales (ACCEFYN), 321–336. doi: 10.18257/raccefyn.25 (96).2001.2796

Amos, C. M., and Castelao, R. M. (2022). Influence of the El Niño-Southern oscillation on SST fronts along the west coasts of north and South America. *J. Geophys. Res.: Oceans.* 127. doi: 10.1029/2022JC018479

Andersson, A. J. (2005). Coastal ocean and carbonate systems in the high CO2 world of the Anthropocene. *Am. J. Sci* 305, 875–918. doi: 10.2475/ajs.305.9.875

Andersson, A. J., and Gledhill, D. (2013). Ocean acidification and coral reefs: effects on breakdown, dissolution, and net ecosystem calcification. *Annu. Rev. Mar. Sci* 5, 321–348. doi: 10.1146/annurev-marine-121211-172241

Bakun, A., and Nelson, C. (1991). The seasonal cycle of wind-stress curl in subtropical eastern boundary current regions. *J. Physical Oceanography* 21 (12), 1815–1834. Available online at: https://journals.ametsoc.org/view/journals/phoc/21/12/1520-0485_1991_021_1815_tscows_2_0_co_2.xml

Bouillon, S. (2011). Storage beneath mangroves. Nature Geoscience 4 (5), 282-283. doi: 10.1038/ngeo1130

Blanco, J. F. (2012). The hydroclimatology of Gorgona Island: seasonal and ENSO-related Patternsa. *Actualidades. Biológicas.* 31, 111–121. doi: 10.17533/udea.acbi.331494

Borges, A. V., and Abril, G. (2011). "Carbon dioxide and methane dynamics in estuaries," in *Treatise on Estuarine and Coastal Science* (Elsevier), 119–161. doi: 10.1016/B978-0-12-374711-2.00504-0

Borges, A. V., Delille, B., and Frankignoulle, M. (2005). Budgeting sinks and sources of CO_2 in the coastal ocean: Diversity of ecosystems counts. *Geophys. Res. Lett.* 32. doi: 10.1029/2005 GL023053

Bravo, L., Ramos, M., Astudillo, O., Dewitte, B., and Goubanova, K. (2016). Seasonal variability of the Ekman transport and pumping in the upwelling system off central-northern Chile (~ 30° S) based on a high-resolution atmospheric regional model (WRF). Ocean. Sci 12, 1049–1065. doi: 10.5194/os-12-1049-2016

Cai, W.-J. (2011). Estuarine and coastal ocean carbon paradox: CO 2 sinks or sites of terrestrial carbon incineration? *Annu. Rev. Mar. Sci* 3, 123–145. doi: 10.1146/annurev-marine-120709-142723

Cai, W.-J., Hu, X., Huang, W.-J., Murrell, M. C., Lehrter, J. C., Lohrenz, S. E., et al. (2011). Acidification of subsurface coastal waters enhanced by eutrophication. *Nat. Geosci.* 4, 766–770. doi: 10.1038/ngeo1297

Cai, W.-J., and Wang, Y. (1998). The chemistry, fluxes, and sources of carbon dioxide in the estuarine waters of the Satilla and Altamaha Rivers, Georgia. *Limnology and Oceanography* 43 (4), 657–668. doi: 10.4319/lo.1998.43.4.0657

Chavez, F. P., Service, S. K., and Buttrey, S. E. (1996). Temperature-nitrate relationships in the central and eastern tropical Pacific. *J. Geophys. Res.: Oceans.* 101, 20553–20563. doi: 10.1029/96JC01943

Chavez, F. P., Strutton, P. G., Friederich, G. E., Feely, R. A., Feldman, G. C., Foley, D. G., et al. (1999). Biological and chemical response of the equatorial pacific ocean to the 1997–98 El Niño. *Science* 286, 2126–2131. doi: 10.1126/science.286.5447.2126

Chen, C.-T. A., and Borges, A. V. (2009). Reconciling opposing views on carbon cycling in the coastal ocean: Continental shelves as sinks and near-shore ecosystems as sources of atmospheric CO₂. *Deep. Sea. Res. Part II.: Topical. Stud. Oceanogr.* 56, 578–590. doi: 10.1016/j.dsr2.2009.01.001

Chen, C., Huang, T. S., Chen, Y., Bai, Y., He, X.-T., and Kang, Y.J. (2013). Air–sea exchanges of $\rm CO_2$ in the world's coastal seas. *Biogeosciences* 10, 6509–6544. doi: 10.5194/bg-10-6509-2013

Chung, C. T. Y., and Power, S. B. (2014). Precipitation response to La Niña and global warming in the Indo-Pacific. *Climate Dynamics*. 43, 3293–3307. doi: 10.1007/s00382-014-2105-9

Clark, J. B., Uz, S. S., Tsontos, V., Huang, T., Scott, J., and Rogers, L. (2022). Assessing carbon properties in coastal waters with a new observing system testbed. *Oceans*, 1–6. doi: 10.1109/OCEANS47191.2022.9977358

Corredor-Acosta, A., Acosta, A., Gaspar, P., and Calmettes, B. (2011). Variation in the surface currents in the Panama Bight during El Nino and LA Nina events from 1993 to 2007. *Bull. Mar. Coast. Res.* 40. doi: 10.25268/bimc.invemar.2011.40.0.127

Corredor-Acosta, A., Cortés-Chong, N., Acosta, A., Pizarro-Koch, M., Vargas, A., Medellín-Mora, J., et al. (2020). Spatio-temporal variability of chlorophyll-A and environmental variables in the Panama bight. *Remote Sens.* 12, 2150. doi: 10.3390/rs12132150

Cosca, C. E., Feely, R. A., Boutin, J., Etcheto, J., McPhaden, M. J., Chavez, F. P., et al. (2003). Seasonal and interannual CO_2 fluxes for the central and eastern equatorial Pacific Ocean as determined from fCO $_2$ -SST relationships. *J. Geophys. Res.: Oceans.* 108. doi: 10.1029/2000JC000677

Courtney, T. A., and Andersson, A. J. (2019). Evaluating measurements of coral reef net ecosystem calcification rates. *Coral. Reefs.* 38, 997–1006. doi: 10.1007/s00338-019-01828-2

Courtney, T. A., Cyronak, T., Griffin, A. J., and Andersson, A. J. (2021). Implications of salinity normalization of seawater total alkalinity in coral reef metabolism studies. *PloS One* 16, e0261210. doi: 10.1371/journal.pone.0261210

Crawford, G., Mepstead, M., and Díaz-Ferguson, E. (2023). Characterizing oceanographic conditions near Coiba Island and Pacific Panama using 20 years of satellite-based wind stress, SST and chlorophyll-a measurements. *Mar. Fish. Sci.* (MAFIS) 37, 391–411. doi: 10.47193/mafis.37X2024010112

Dai, X., Ma, J., Zhang, H., and Xu, W. (2013). Evaluation of ecosystem health for the coastal wetlands at the Yangtze Estuary, Shanghai. *Wetlands. Ecol. Manage.* 21, 433–445. doi: 10.1007/s11273-013-9316-4

Dai, M., Su, J., Zhao, Y., Hofmann, E. E., Cao, Z., Cai, W.-J., et al. (2022). Carbon fluxes in the coastal ocean: synthesis, boundary processes, and future trends. *Annu. Rev. Earth Planet. Sci.* 50, 593–626. doi: 10.1146/annurev-earth-032320-090746

DeGrandpre, M. D., Hammar, T. R., and Wirick, C. D. (1998). Short-term pCO₂ and O₂ dynamics in California coastal waters. *Deep. Sea. Res. Part II.: Topical. Stud. Oceanogr.* 45, 1557–1575. doi: 10.1016/S0967-0645(98)80006-4

Devis-Morales, A., Schneider, W., Montoya-Sánchez, R. A., and Rodríguez Rubio, E. (2008). Monsoon-like winds reverse oceanic circulation in the Panama Bight. *Geophys. Res. Lett.* 35, L20607. doi: 10.1029/2008GL035172

Diaz, R. J. (2001). Overview of hypoxia around the world. *J. Environ. Qual.* 30, 275–281. doi: 10.2134/jeq2001.302275x

Díaz Guevara, D. C., Málikov, I., and Villegas Bolaños, N. L. (2008). Características de las zonas de surgencia de la cuenca del Pacífico Colombiano y su relación con la zona de convergencia intertropical. *Boletín. Científico. CIOH.* 26, 59–71. doi: 10.26640/01200542.26.59

Dickson, A. G. (1990). Standard potential of the reaction: AgCl (s)+ 12H2 (g)= Ag (s) + HCl (aq), and the standard acidity constant of the ion HSO_4 – in synthetic sea water from 273.15 to 318.15 K. J. Chem. Thermodynamics. 22, 113–127. doi: 10.1016/0021-9614(90)90074-z

Dickson, A. G., Sabine, C. L., and Christian, J. R. (Eds.) (2007). Guide to best practices for ocean CO_2 measurements (PICES Special Publication 3), 191. ("Guide" in one PDF file). Available online at: https://www.ncei.noaa.gov/access/ocean-carbonacidification-data-system/oceans/Handbook_2007/Guide_all_in_one.pdf

Doney, S. C., Lima, I., Feely, R. A., Glover, D. M., Lindsay, K., Mahowald, N., et al. (2009b). Mechanisms governing interannual variability in upper-ocean inorganic carbon system and air–sea $\rm CO_2$ fluxes: Physical climate and atmospheric dust. *Deep. Sea. Res. Part II.: Topical. Stud. Oceanogr.* 56, 640–655. doi: 10.1016/j.dsr2.2008.12.006

Else, B. G. T., Papakyriakou, T. N., Galley, R. J., Mucci, A., Gosselin, M., Miller, L. A., et al. (2013). Annual cycle of air–sea $\rm CO_2$ exchange in an Arctic Polynya region. *J. Geophys. Res.: Biogeosci.* 118, 681–703. doi: 10.1002/jgrg.20023

Engel, A., Kiko, R., and Dengler, M. (2022). Organic matter supply and utilization in oxygen minimum zones. *Annu. Rev. Mar. Sci* 14, 355–378. doi: 10.1146/annurev-marine-041921-090849

Fabre, C., Sauvage, S., Probst, J.-L., and Sánchez-Pérez, J. M. (2020). Global-scale daily riverine DOC fluxes from lands to the oceans with a generic model. *Global and Planetary Change* 194, 103294. doi: 10.1016/j.gloplacha.2020.103294

Feely, R., Doney, S., and Cooley, S. (2009). Ocean acidification: present conditions and future changes in a high-CO₂ world. *Oceanography* 22, 36–47. doi: 10.5670/oceanog.2009.95

Feely, R. A., Takahashi, T., Wanninkhof, R., McPhaden, M. J., Cosca, C. E., Sutherland, S. C., et al. (2006). Decadal variability of the air-sea CO_2 fluxes in the equatorial Pacific Ocean. *J. Geophys. Res.: Oceans.* 111. doi: 10.1029/2005JC003129

Feely, R. A., Wanninkhof, R., McGillis, W., Carr, M.-E., and Cosca, C. E. (2004). Effects of wind speed and gas exchange parameterizations on the air-sea CO₂ fluxes in the equatorial Pacific Ocean. *J. Geophys. Res.: Oceans.* 109. doi: 10.1029/2003JC001896

Fiedler, P. C., and Lavín, M. F. (2017). Oceanographic Conditions of the Eastern Tropical Pacific. Berlin: Springer Nature Link 59–83. doi: 10.1007/978-94-017-7499-4_3

Ford, D. J., Tilstone, G. H., Shutler, J. D., and Kitidis, V. (2022). Identifying the biological control of the annual and multi-year variations in South Atlantic air–sea CO_2 flux. *Biogeosciences* 19, 4287–4304. doi: 10.5194/bg-19-4287-2022

Friedlingstein, P., O'Sullivan, M., Jones, M. W., Andrew, R. M., Bakker, D. C. E., Hauck, J., et al. (2023). Global carbon budget 2023. *Earth Syst. Sci Data* 15, 5301–5369. doi: 10.5194/essd-15-5301-2023

Gan, J., Li, L., Wang, D., and Guo, X. (2009). Interaction of a river plume with coastal upwelling in the northeastern South China Sea. *Continent. Shelf. Res.* 29, 728–740. doi: 10.1016/j.csr.2008.12.002

Gassen, L., Esters, L., Ribas-Ribas, M., and Wurl, O. (2024). The impact of rainfall on the sea surface salinity: a mesocosm study. *Sci. Rep.* 14, 6353. doi: 10.1038/s41598-024-5015.4

Gerrard, M. B. (2023). "The role of ocean CDR in mitigating climate change," in *Ocean Carbon Dioxide Removal for Climate Mitigation* (Edward Elgar Publishing), 12–19. doi: 10.4337/9781802208856.00009

Giraldo, A., Rodríguez-Rubio, E., and Zapata, F. (2008). Condiciones oceanográficas en isla Gorgona, Pacífico oriental tropical de Colombia. *Latin. Am. J. Aquat. Res.* 36, 121–128. doi: 10.3856/vol36-issue1-fulltext-12

Giraldo, A., Valencia, B., and Ramírez, D. G. (2011). Productividad planctónica y condiciones oceanográficas locales en Isla Gorgona durante julio 2006. *Bol. Invest. Mar. Cost.* 40, 185–201. doi: 10.25268/bimc.invemar.2011.40.1.108

Giraldo López, A. (2008). Variabilidad espacial de temperatura, salinidad y transparencia en el ambiente pelágico del PNN Gorgona durante septiembre 2007 y marzo 2008. *Boletín. Científico. CIOH.* 26, 157–163. doi: 10.26640/22159045.192

Guzmán, D. H., Mier, R. L., Vergara, A., and Milanes, C. B. (2023). Marine protected areas in Colombia: A historical review of legal marine protection since the late 1960s to 2023. *Marine Policy*, 155, 105726. doi: 10.1016/j.marpol.2023.105726

Hans-Rolf, D., and Fritz, V. (2023). Oceans' surface pH-value as an example of a reversible natural response to an anthropogenic perturbation. *Ann. Mar. Sci* 7, 034–039. doi: 10.17352/ams.000036

Herrera Carmona, J. C., Selvaraj, J. J., and Giraldo, A. (2022). Dynamic regionalization of the Panama Bight, Eastern Tropical Pacific, using remote sensing data. *Int. J. Remote Sens.* 43, 3131–3151. doi: 10.1080/01431161.2022.2063040

Hu, J., Lan, W., Huang, B., Chiang, K.-P., and Hong, H. (2015). Low nutrient and high chlorophyll a coastal upwelling system – A case study in the southern Taiwan Strait. *Estuarine. Coast. Shelf. Sci* 166, 170–177. doi: 10.1016/j.ecss.2015.05.020

Huang, J., Li, Q., Wu, P., Wang, S., Gu, S., Guo, M., et al. (2022). The buffering of a riverine carbonate system under the input of acid mine drainage: Example from a small karst watershed, southwest China. *Front. Environ. Sci.* 10 doi: 10.3389/fenys.2022.1020452

Hydes, D., Jiang, Z.-P., Hartman, M. C., Campbell, J. M., Hartman, S. E., Pagnani, M. R., et al. (2012). Surface DIC and TALK measurements along the M/V Pacific Celebes VOS Line during the 2007–2012 cruises. Carbon Dioxide Information Analysis Center, Oak Ridge National Laboratory, US Department of Energy, Oak Ridge, TN. doi: 10.3334/CDIAC/OTG.VOS_PC_2007-2012

Ianson, D., Feely, R. A., Sabine, C. L., and Juranek, L. W. (2009). Features of coastal upwelling regions that determine net air-sea $\rm CO_2$ flux. J. Oceanogr. 65, 677–687. doi: 10.1007/s10872-009-0059-z

INVEMAR. (2019). Informe del Estado de los Ambientes Marinos y Costeros en Colombia 2019 (Santa Marta: Instituto de Investigaciones Marinas y Costeras INVEMAR). Available online at: https://portal.invemar.org.co/inf-ier (Accessed July 28, 2023).

INVEMAR. (2020). Informe del Estado de los Ambientes Marinos y Costeros en Colombia 2020 (Santa Marta: Instituto de Investigaciones Marinas y Costeras INVEMAR). Available online at: https://portal.invemar.org.co/inf-ier (Accessed July 28, 2023).

INVEMAR. (2022). Informe del Estado de los Ambientes Marinos y Costeros en Colombia 2022 (Santa Marta: Instituto de Investigaciones Marinas y Costeras INVEMAR). Available online at: https://portal.invemar.org.co/inf-ier (Accessed July 28. 2023).

Jersild, A., Landschützer, P., Gruber, N., and Bakker, D. C. E. (2017). An observation-based global monthly gridded sea surface pCO_2 and air–sea CO_2 flux product from 1982 onward (NCEI Accession 0160558). NOAA National Centers for Environmental Information. doi: 10.7289/V5Z899N6

Jiang, Z.-P., Tyrrell, T., Hydes, D. J., Dai, M., and Hartman, S. E. (2014). Variability of alkalinity and the alkalinity-salinity relationship in the tropical and subtropical surface ocean, Global Biogeochem. Cycles~28,~729-742.~doi:~10.1002/2013GB004678

Johnson, M. S., Billett, M. F., Dinsmore, K. J., Wallin, M., Dyson, K. E., and Jassal, R. S. (2010). Direct and continuous measurement of dissolved carbon dioxide in freshwater aquatic systems—method and applications. *Ecohydrology* 3, 68–78. doi: 10.1002/eco.95

Johnson, K., Sieburth, J. M., Williams, P.J. le., and Brändström, L. (1987). Coulometric total carbon dioxide analysis for marine studies: Automation and calibration. *Mar. Chem.* 21, 117–133. doi: 10.1016/0304-4203(87)90033-8

Kahl, L. C. (2018). Dinámica del CO_2 en el Océano Atlántico Sudoccidental (Buenos Aires, Argentina: Universidad de Buenos Aires, Facultad de Ciencias Exactas y Naturales). Available online at: https://hdl.handle.net/20.500.12110/tesis_n6525_Kahl (Accessed May 17, 2025).

Kao, H.-Y., and Yu, J.-Y. (2009). Contrasting eastern-pacific and central-pacific types of ENSO. $J.\ Climate\ 22,\ 615-632.\ doi:\ 10.1175/2008jcli2309.1$

Kawabe, M., and Fujio, S. (2010). Pacific Ocean circulation based on observation. J. Oceanogr. 66, 389–403. doi: 10.1007/s10872-010-0034-8

Kessler, W. S. (2006). The circulation of the eastern tropical Pacific: A review. *Prog. Oceanogr.* 69, 181–217. doi: 10.1016/j.pocean.2006.03.009

Kim, D., Choi, Y., Kim, T.-W., and Park, G.-H. (2017). Recent increase in surface fCO $_2$ in the western subtropical North Pacific. *Ocean. Sci J.* 52, 329–335. doi: 10.1007/s12601-017-0030-7

Kim, H. J., Kim, T., Hyeong, K., Yeh, S., Park, J., Yoo, C. M., et al. (2019). Suppressed CO₂ outgassing by an enhanced biological pump in the eastern tropical pacific. *J. Geophys. Res.: Oceans.* 124, 7962–7973. doi: 10.1029/2019JC015287

Körtzinger, A. (2003). A significant CO2 sink in the tropical Atlantic Ocean associated with the Amazon River plume. *Geophysical Research Letters* 30 (24), 2287. doi: 10.1029/2003GL018841

Kryzhova, K. A., and Semkin, P. Y. (2023). Carbonate System and CO₂ Fluxes in the Partizanskaya River Estuary. Berlin: Springer Nature Link 268–279. doi: 10.1007/978-3-031-47851-2_32

Lal, R. B. (2024). Recent trends in carbon sequestration technique. *J. Biochemical Sciences*. doi: 10.61577/jbs.2024.100003

Landschützer, P., Gruber, N., and Bakker, D. C. E. (2016). Decadal variations and trends of the global ocean carbon sink. *Global Biogeochem. Cycles.* 30, 1396–1417. doi: 10.1002/2015GB005359

 $Landschützer, P., Keppler, L., and Ilyina, T. (2022). \textit{Ocean systems} \ (Elsevier eBooks), 427-452. \ doi: 10.1016/b978-0-12-814952-2.00004-6$

Lanson, D., Feely, R. A., Sabine, C. L., and Juranek, L. W. (2009). Features of coastal upwelling regions that determine net air–sea CO2 flux. *J. Oceanography* 65 (5), 677–687. doi: 10.1007/s10872-009-0059-z

Laruelle, G. G., Dürr, H. H., Slomp, C. P., Borges, A. V., Gypens, N., Lauerwald, R., et al. (2013). Air–sea CO2 exchanges in the world's coastal seas. *Biogeosciences* 10, 6509–6544. doi: 10.5194/bg-10-6509-2013

Lee, K., Kim, T. W., Byrne, R. H., Millero, F. J., Feely, R. A., and Liu, Y. M. (2010). The universal ratio of boron to chlorinity for the North Pacific and North Atlantic oceans. *Geochim. Cosmochim. Acta* 74, 1801–1811. doi: 10.1016/j.gca.2009.12.027

Legge, O. J., Bakker, D. C. E., Johnson, M. T., Meredith, M. P., Venables, H. J., Brown, P. J., et al. (2015). The seasonal cycle of ocean-atmosphere CO₂ flux in Ryder Bay, west Antarctic Peninsula. *Geophys. Res. Lett.* 42, 2934–2942. doi: 10.1002/2015GL063796

Lewis, E., and Wallace, (1998). Program Developed for CO_2 System Calculations OSTI OAI (U.S. Department of Energy Office of Scientific and Technical Information). doi: 10.15485/1464255

Li, J., Cao, R., Lao, Q., Chen, F., Chen, C., Zhou, X., et al. (2020). Assessing seasonal nitrate contamination by nitrate dual isotopes in a monsoon-controlled bay with intensive human activities in South China. *Int. J. Environ. Res. Public Health* 17, 1921. doi: 10.3390/jierph17061921

Li, H., Zhang, J., Xuan, J., Wu, Z., Ran, L., Wiesner, M. G., et al. (2022). Asymmetric response of the biological carbon pump to the ENSO in the south China sea. *Geophys. Res. Lett.* 49. doi: 10.1029/2021gl095254

Liss, P. S., and Merlivat, L. (1986). Air–sea gas exchange rates: Introduction and synthesis, in P. Buat-Ménard (ed.), *The Role of Air–Sea Exchange in Geochemical Cycling*, NATO ASI Series (Series C: Mathematical and Physical Sciences), vol. 185, Springer, Dordrecht, 113–127. doi: 10.1007/978-94-009-4738-2_5

Lorenzoni, L., Hu, C., Varela, R., Arias, G., Guzmán, L., and Muller-Karger, F. (2011). Bio-optical characteristics of Cariaco Basin (Caribbean Sea) waters. *Continent. Shelf. Res.* 31, 582–593. doi: 10.1016/j.csr.2010.12.013

Macdonald, H. S., Baird, M. E., and Middleton, J. H. (2009). Effect of wind on continental shelf carbon fluxes off southeast Australia: A numerical model. *J. Geophys. Res.: Oceans.* 114. doi: 10.1029/2008JC004946

McKee, B. A., Aller, R. C., Allison, M. A., Bianchi, T. S., and Kineke, G. C. (2004). Transport and transformation of dissolved and particulate materials on continental margins influenced by major rivers: benthic boundary layer and seabed processes. *Continent. Shelf. Res.* 24, 899–926. doi: 10.1016/j.csr.2004.02.009

McKinley, G. A., Fay, A. R., Eddebbar, Y. A., Gloege, L., and Lovenduski, N. S. (2020). External forcing explains recent decadal variability of the ocean carbon sink. $AGU.\ Adv.\ 1.\ doi: 10.1029/2019AV000149$

McLean, P., Bulmer, C., Davies, P., Dunstone, N., Gordon, M., Ineson, S., et al. (2024). Predictability of European winter 2021/2022: Influence of La Niña and stratospheric polar vortex. *Atmospher. Sci Lett.* 25. doi: 10.1002/asl.1255

Miller, L. A., Shadwick, E. H., and Thomas, H. (2019). Air–sea $\rm CO_2$ fluxes in the Hudson Bay system: The role of stratification. *Geophys. Res. Lett.* 46, 541–549. doi: 10.1029/2018 GL080099

Millero, F. J. (2010). Carbonate constants for estuarine waters. Mar. Freshw. Res. 61, 139–142. doi: 10.1071/mf09254

Millero, F. J., Degler, E. A., O'Sullivan, D. W., Goyet, C., and Eischeid, G. (1998). The carbon dioxide system in the Arabian Sea. *Deep Sea Research Part II* 45, 2225–2252.

Millero, F. J., Lee, K., and Roche, M. P. (1998). Distribution of alkalinity in the surface waters of the major oceans. *Marine Chemistry* 60 (1–2), 111–130. doi: 10.1016/S0304-4203(97)00084-4

Monteiro, T., Batista, M., Henley, S., MaChado, E., da, C., Araujo, M., et al. (2022). Contrasting sea-air CO₂ exchanges in the western tropical atlantic ocean. *Global Biogeochem. Cycles.* 36. doi: 10.1029/2022GB007385

Mu, L., Gruber, N., and Doney, S. C. (2020). Seasonality of air–sea CO₂ fluxes in the Arctic Ocean: The role of sea ice, freshwater input, and biological uptake. *Global Biogeochem. Cycles.* 34, e2020GB006574. doi: 10.1029/2020GB006574

Murcia Riaño, M., and Giraldo López, A. (2007). Condiciones oceanográficas y composición del Mesozooplancton en la zona oceánica del Pacífico Colombiano, durante septiembre-octubre 2004. *Boletín. Científico. CCCP.* 14, 83–94. doi: 10.26640/01213423.14.83_94

NOAA. (2021). Mauna Loa CO₂ monthly mean data. NOAA Global Monitoring Laboratory. Available online at: https://gml.noaa.gov/ccgg/trends/data.html (Accessed September 2022)

NOAA. (2022). Mauna Loa CO₂ monthly mean data. NOAA Global Monitoring Laboratory. Available online at: https://gml.noaa.gov/ccgg/trends/data.html (Accessed September 2022)

Olafsson, J., Olafsdottir, S. R., Takahashi, T., Danielsen, M., and Arnarson, T. S. (2021). Enhancement of the north atlantic CO_2 sink by arctic waters. *Biogeosciences* 18, 1689–1701. doi: 10.5194/bg-18-1689-2021

Oliveira, A. P., Fernandes, A. M., Fonseca, V. F., Vale, C., and Mendonça, A. M. M. (2017). Inorganic carbon distribution and $\rm CO_2$ fluxes in a large tropical estuary (Tagus, Portugal). *Scientific Reports*. doi: 10.1038/s41598-017-06758-z

Palacios Moreno, M. A., and Pinto Tovar, C. A. (1992). Estudio de la influencia de la marea en el río Guapi. *Boletín. Científico. CCCP.* 3, 3–13. doi: 10.26640/01213423.3.3_13

Palacios Peñaranda, M. L., Cantera Kintz, J. R., and Peña Salamanca, E. J. (2019). Carbon stocks in mangrove forests of the Colombian Pacific. *Estuarine. Coast. Shelf. Sci* 227, 106299. doi: 10.1016/j.ecss.2019.106299

Park, G.-H., Wanninkhof, R., Doney, S. C., Takahashi, T., Lee, K., Feely, R. A., et al. (2010). Variability of global net sea air CO₂: fluxes over the last three decades using empirical relationships. *Tellus. B.: Chem. Phys. Meteorol.* 62, 352. doi: 10.1111/j.1600-0889.2010.00498.x

Parv, S., Chen, Z., Shutler, J., and Watson, A.. (2023). Assessing Air–sea CO2 flux products with constraints from atmospheric inverse analyses. *EGU General Assembly* 2023. doi: 10.5194/egusphere-egu23-10224

Pasquero, C., Bracco, A., and Provenzale, A. (2005). Impact of the spatiotemporal variability of the nutrient flux on primary productivity in the ocean. *J. Geophys. Res.: Oceans.* 110. doi: 10.1029/2004JC002738

Paulmier, A., Ruiz-Pino, D., and Garçon, V. (2011). CO₂ maximum in the oxygen minimum zone (OMZ). *Biogeosciences* 8, pp.239–pp.252. doi: 10.5194/bg-8-239-2011

Peng, C., Crawshaw, J. P., Maitland, G. C., Martin Trusler, J. P., and Vega-Maza, D. (2013). The pH of $\rm CO_2$ -saturated water at temperatures between 308K and 423K at pressures up to 15MPa. *J. Supercrit. Fluids.* 82, 129–137. doi: 10.1016/j.supflu.2013.07.001

Perez, F. F., and Fraga, F. (2003). Association constant of fluoride and hydrogen ions in seawater. *Mar. Chem.* 21, 161–168. doi: 10.1016/0304-4203(87)90036-3

Pierrot, D., Epitalon, J.-M., Orr, J. C., and Lewis, E. R. (2021). and Wallace, D.: MS Excel program developed for CO₂ system calculations – version 3.0. Available online at: https://github.com/dpierrot/co2sys_xl (Accessed May 17, 2025).

Polavarapu, S. M., Deng, F., Byrne, B., Jones, D. B. A., and Neish, M. (2018). A comparison of atmospheric CO2 flux signals obtained from GEOS-Chem flux inversions constrained by in situ or GOSAT observations. doi: 10.5194/acp-2017-1235

Prytherch, J., Yelland, M. J., Pascal, R. W., Moat, B. I., Skjelvan, I., and Srokosz, M. A. (2010). Open ocean gas transfer velocity derived from long-term direct measurements of the CO₂ flux. *Geophys. Res. Lett.* 37. doi: 10.1029/2010GL045597

Quiñones-Rivera, Z. J., Wissel, B., Turner, R. E., Rabalais, N. N., Justić, D., Finlay, K. P., et al. (2022). Divergent effects of biological and physical processes on dissolved oxygen and dissolved inorganic carbon dynamics on a eutrophied and hypoxic continental shelf. *Limnol. Oceanogr.* 67, 2603–2616. doi: 10.1002/lno.12225

Ramaekers, L., Vanschoenwinkel, B., Brendonck, L., and Pinceel, T. (2023). Elevated dissolved carbon dioxide and associated acidification delays maturation and decreases calcification and survival in the freshwater crustacean Daphnia magna. *Limnol. Oceanogr.* 68, 1624–1635. doi: 10.1002/lno.12372

Rastogi, B., Miller, J. B., Trudeau, M., Andrews, A. E., Hu, L., Mountain, M., et al. (2021). Evaluating consistency between total column CO2 retrievals from OCO-2 and the in situ network over North America: implications for carbon flux estimation. *Atmospheric Chemistry and Physics* 21 (18), 14385–14401. doi: 10.5194/acp-21-14385-2021

Reimer, J. J., Vargas, R., Smith, S. V., Lara-Lara, R., Gaxiola-Castro, G., Martín Hernández-Ayón, J., et al. (2013). Air-sea CO₂ fluxes in the near-shore and intertidal zones influenced by the California Current. *J. Geophys. Res.: Oceans.* 118, 4795–4810. doi: 10.1002/jgrc.20319

Restrepo, J. D., and Kjerfve, B. (2004). "The pacific and caribbean rivers of Colombia: water discharge, sediment transport and dissolved loads," in *Environmental Geochemistry in Tropical and Subtropical Environments* (Springer Berlin Heidelberg), 169–187. doi: 10.1007/978-3-662-07060-4 14

Ricaurte-Villota, C., Murcia-Riaño, M., and Hernádez-Ayón, J. M. (2025). Dynamics and drivers of the carbonate system: response to terrestrial runoff and upwelling along the Northeastern Colombian Caribbean coast. *Front. Mar. Sci* 11. doi: 10.3389/fmars.2024.1305542

Ries, J. B., Cohen, A. L., and McCorkle, D. C. (2009). Marine calcifiers exhibit mixed responses to CO₂-induced Ocean acidification. *Geology* 37, 1131–1134. doi: 10.1130/G30210A.1

Rodríguez-Rubio, E., Schneider, W., and Abarca del Río, R. (2003). On the seasonal circulation within the Panama Bight derived from satellite observations of wind, altimetry and sea surface temperature. *Geophys. Res. Lett.* 30. doi: 10.1029/2002GL016794

Roobaert, A., Goulven, L., Resplandy, L., Landschützer, P., Gruber, N., Liao, E., et al. (2021). The spatiotemporal dynamics of the sources and sinks of CO2 in the global coastal ocean. MPG.PuRe (Max Planck Society). doi: 10.5194/egusphere-egu21-10048

Roobaert, A., Regnier, P., Landschützer, P., and Laruelle, G. G. (2024). A novel sea surface pCO₂-product for the global coastal ocean resolving trends over 1982–2020. *Earth Syst. Sci Data* 16, 421–441. doi: 10.5194/essd-16-421-2024

Roobaert, A., Regnier, P., Landschützer, P., and Laruelle, G. G. (2025). Global coastal ocean $\rm CO_2$ trends over the 1982–2020 period. doi: 10.5194/egusphere-egu24-14775

Rosentreter, J. A., Laruelle, G. G., Bange, H. W., Bianchi, T. S., Busecke, J. J. M., Cai, W.-J., et al. (2023). Coastal vegetation and estuaries are collectively a greenhouse gas sink. *Nat. Climate Change* 13, 579–587. doi: 10.1038/s41558-023-01682-9

Santos, I. R., Hatje, V., Serrano, O., Bastviken, D., and Krause-Jensen, D. (2022). Carbon sequestration in aquatic ecosystems: Recent advances and challenges. *Limnol. Oceanogr.* 67. doi: 10.1002/lno.12268

Saraswat, R. (2011). "Global equatorial sea-surface temperatures over the last 150,000 years: an update from foraminiferal elemental analysis," in *current science*, vol. 100. Bangalore, India: Current Science, 1201–1206.

Schneider, T., Bischoff, T., and Haug, G. H. (2014). Migrations and dynamics of the intertropical convergence zone. *Nature* 513, 45–53. doi: 10.1038/nature13636

Séférian, R., Bopp, L., Swingedouw, D., and Servonnat, J. (2013). Dynamical and biogeochemical control on the decadal variability of ocean carbon fluxes. *Earth Syst. Dynamics.* 4, 109–127. doi: 10.5194/esd-4-109-2013

Smith, S. V., and Hollibaugh, J. T. (1993). Coastal metabolism and the oceanic organic carbon balance. *Rev. Geophys.* 31, 75–89. doi: 10.1029/92RG02584

Stevenson, M. (1970). Circulation in the Panama bight. *J. Geophys. Res.* 75, 659–672. doi: 10.1029/IC075i003p00659

Strutton, P. G., Evans, W., and Chavez, F. P. (2008). Equatorial Pacific chemical and biological variability 1997–2003. *Global Biogeochem. Cycles.* 22. doi: 10.1029/2007GB003045

Sun, Q., Li, D., Wang, B., Xu, Z., Miao, Y., Lin, H., et al. (2023). Massive nutrients offshore transport off the Changjiang Estuary in flooding summer of 2020. *Front. Mar. Sci* 10. doi: 10.3389/fmars.2023.1076336

Swesi, A., Yusup, Y., Ahmad, M. I., Almdhun, H. M., Jamshidi, E. J., Sigid, M. F., et al. (2023). Seasonal and yearly controls of CO_2 fluxes in a tropical coastal ocean. *Earth Interact.* 27. doi: 10.1175/EI-D-22-0023.1

Takahashi, T., Feely, R. A., Weiss, R. F., Wanninkhof, R. H., Chipman, D. W., Sutherland, S. C., et al. (1997). Global air-sea flux of CO₂: An estimate based on measurements of sea-air pCO₂ difference. *Proc. Natl. Acad. Sci.* 94, 8292–8299. doi: 10.1073/pnas.94.16.8292

Takahashi, T., Sutherland, S. C., Sweeney, C., Poisson, A., Metzl, N., Tilbrook, B., et al. (2002). Global sea–air CO_2 flux based on climatological surface ocean pCO_2 , and seasonal biological and temperature effects. *Deep. Sea. Res. Part II.: Topical. Stud. Oceanogr.* 49, 1601–1622. doi: 10.1016/S0967-0645(02)00003-6

Tide-Forecast.com (2022). Map of tide Stations in Colombia. Available online at: https://www.tide-forecast.com/weather_maps/Colombia (Accessed May 17, 2025).

Tomczak, M. (1981). A multi-parameter extension of temperature/salinity diagram techniques for the analysis of non-isopycnal mixing. *Prog. Oceanogr.* 10, 147–171. doi: 10.1016/0079-6611(81)90010-0

Torres, R. R., Giraldo, E., Muñoz, C., Caicedo, A., Hernández-Carrasco, I., and Orfila, A. (2023). Seasonal and El Niño-Southern oscillation-related ocean variability in the Panama bight. *Ocean. Sci* 19, 685–701. doi: 10.5194/os-19-685-2023

UAESPNN (2005). Parque Nacional Natural Gorgona: Plan de Manejo 2005–2009 (Cali: Unidad Administrativa Especial del Sistema de Parques Nacionales Naturales de Colombia). Available online at: https://koha.parquesnacionales.gov.co/cgi-bin/koha/opac-detail.pl?biblionumber=3899 (Accessed May 17, 2025).

Vaittinada Ayar, P., Bopp, L., Christian, J. R., Ilyina, T., Krasting, J. P., Séférian, R., et al. (2022). Contrasting projections of the ENSO-driven $\rm CO_2$ flux variability in the equatorial Pacific under high-warming scenario. *Earth Syst. Dynamics.* 13, 1097–1118. doi: 10.5194/esd-13-1097-2022

Vargas, C. A., Martínez, R. A., Cuevas, L. A., Pavez, M. A., Cartes, C., GonzÁlez, H. E., et al. (2007). The relative importance of microbial and classical food webs in a highly productive coastal upwelling area. *Limnol. Oceanogr.* 52, 1495–1510. doi: 10.4319/lo.2007.52.4.1495

Wang, D., Wang, H., Li, M., Liu, G., and Wu, X. (2013). Role of Ekman transport versus Ekman pumping in driving summer upwelling in the South China Sea. *J. Ocean. Univ. China* 12, 355–365. doi: 10.1007/s11802-013-1904-7

Wang, J., Zeng, N., Wang, M., Jiang, F., Wang, H., and Jiang, Z. (2018). Contrasting terrestrial carbon cycle responses to the 1997/98 and 2015/16 extreme El Niño events. *Earth Syst. Dynamics.* 9, 1–14. doi: 10.5194/esd-9-1-2018

Wanninkhof, R. (2014). Relationship between wind speed and gas exchange over the ocean revisited. *Limnology and Oceanography: Methods* 12, 351–362. doi: 10.4319/lom.2014.12.351

Watanabe, K., Tokoro, T., Moki, H., and Kuwae, T. (2024). Contribution of marine macrophytes to pCO_2 and DOC variations in human-impacted coastal waters. Biogeochemistry 167, 831–848. doi: 10.1007/s10533-024-01140-4

Weber, E. D., Auth, T. D., Baumann-Pickering, S., Baumgartner, T. R., Bjorkstedt, E. P., Bograd, S. J., et al. (2021). State of the California current 2019–2020: back to the future with marine heatwaves? *Front. Mar. Sci* 8. doi: 10.3389/fmars.2021.709454

Weiss, R. F. (1974). Carbon dioxide in water and seawater: the solubility of a non-ideal gas. *Mar. Chem.* 2, 203–215. doi: 10.1016/0304-4203(74)90015-2

Willett, C. S., Leben, R. R., and Lavín, M. F. (2006). Eddies and Tropical Instability Waves in the eastern tropical Pacific: A review. *Prog. Oceanogr.* 69, 218–238. doi: 10.1016/j.pocean.2006.03.010

Williams, R. G., and Follows, M. J. (2003). "Physical transport of nutrients and the maintenance of biological production," in *Ocean biogeochemistry: The role of the ocean carbon cycle in global change* (Springer Berlin Heidelberg, Berlin, Heidelberg), 19–51.

Wong, S. C. K., McKinley, G. A., and Seager, R. (2022). Equatorial pacific pCO₂ interannual variability in CMIP6 models. *J. Geophys. Res.: Biogeosci.* 127. doi: 10.1029/2021G007243

Yilmaz, E., Bernardello, R., and Martin, A. P. (2022). Natural processes behind the CO₂ sink variability in the Southern Ocean during the last three decades. Göttingen, Germany: Copernicus GmbH doi: 10.5194/egusphere-egu22-7827

Zhai, W., Dai, M., Cai, W.-J., Wang, Y., and Hong, H. (2005). The partial pressure of carbon dioxide and air–sea fluxes in the northern South China Sea in spring, summer and autumn. *Mar. Chem.* 96, 87–97. doi: 10.1016/j.marchem.2004.12.002